Research Square

Preprints are preliminary reports that have not undergone peer review.
They should not be considered conclusive, used to inform clinical practice,
or referenced by the media as validated information.

Targeted modulation of phosphate and lipid metabolism reduces ligament mineralization in col9a1b knockout models

Erika Kague

ekague@ed.ac.uk

University of Edinburgh https://orcid.org/0000-0002-0266-9424

Batriz Larraz-Prieto

Renata Raele

https://orcid.org/0000-0002-2002-0864

Joanna Moss

University of Bristol https://orcid.org/0000-0003-1690-6512

Chrissy Hammond

University of Bristol https://orcid.org/0000-0002-4935-6724

Article

Keywords: intervertebral disc degeneration, collagen IX (col9), zebrafish, phosphate, lipid metabolism, notochord

Posted Date: July 22nd, 2025

DOI: https://doi.org/10.21203/rs.3.rs-7082517/v1

License: This work is licensed under a Creative Commons Attribution 4.0 International License.
Read Full License

Additional Declarations: There is **NO** Competing Interest.

Targeted modulation of phosphate and lipid metabolism reduces ligament mineralization in *col9a1b* knockout models

Authors: Erika Kague[1, 2]*, Beatriz Larraz-Pieto[2], Renata A. Raele[1], Joanna Moss[1], and Chrissy L Hammond[1]*

Affiliations:

1- School of Physiology, Pharmacology and Neuroscience, Biomedical Sciences, University of Bristol, BS8 1TD, UK.

2- Institute of Genetic and Cancer, University of Edinburgh, Edinburgh, United Kingdom

*Correspondence to: chrissy.hammond@bristol.ac.uk and erika.kague@bristol.ac.uk

Key words: intervertebral disc degeneration, collagen IX (col9), zebrafish, phosphate, lipid metabolism, notochord

Abstract

Intervertebral disc degeneration (IVDD) is a major global cause of chronic back pain and disability in the aging population, characterized by disc matrix breakdown, ligament mineralization, and pain. Effective pharmacological treatments for IVDD are currently unavailable. We used *col9a1b* mutant zebrafish to elucidate the genetic and molecular mechanisms of disc disease, with a focus on ectopic mineralization. We found that *col9a1b* mutants exhibit ectopic intervertebral ligament mineralization, vertebral fusions, and disc degeneration, mirroring human IVDD. Histological, electron microscopy, and molecular analyses revealed that structural disorganization of the notochord epithelium underpins these vertebral fusions. Transcriptomic profiling implicated dysregulation of lipid metabolism and mTOR signalling in ligament biomineralization and vertebral column degeneration in the mutants. Pharmacological interventions targeting phosphate buffering, retinoic acid, lipid metabolism, and mTOR signalling successfully reduced vertebral fusion events. Notably, bisphosphonates and calorie restriction demonstrated superior efficacy in reducing ligament mineralization. Our findings establish *col9a1b* zebrafish mutants as a valuable model for investigating ligament mineralization and vertebral column degeneration, while identifying promising therapeutic targets, including phosphate and lipid metabolism pathways.

Introduction

It is estimated that 80% of the world population will suffer from symptoms of back pain at some moment of their lives [1]. Chronic back and neck pain are the top causes of years lived with disability and heath care costs worldwide [2]. Despite the important public health issue, the pathophysiology of back pain remains largely undetermined. A major cause of back pain is intervertebral disc degeneration (IVDD), which is considered one of the first pathological signs and a potential target for intervention. In the US, over $100 billion is estimated to be spent annually on direct and indirect costs of IVDD and back pain [2]. Despite the high socioeconomic burden of IVDD, there are no disease-modifiable therapies, and surgery remains the only option for long-term alleviation of pain [3].

IVDD comprise of a broad spectrum of phenotypes associated with the IVD, such as fibrosis, ectopic mineralization, herniation, or mixed phenotypes. The aetiology of IVDD is complex with environmental (obesity, smoking, injury, mechanical overload, etc) and genetic influences, but over the last few decades, it has become clear that genetic factors are a major risk [4]. Linkage studies and, more recently, genome-wide association studies (GWAS) have highlighted genes associated with IVDD, such as *THBSs* (thrombospondin proteins) [5, 6], *VDR* (Vitamin D receptor) [7, 8], *GDF5*, interleukins, and collagens (types I, II, III, IX, and XI) [9, 10]. Uncovering the precise mechanisms of how genetic factors lead to IVDD susceptibility and vertebral column degeneration represent opportunities for potential therapeutic pathways.

Intervertebral discs (IVDs) are located between vertebral bodies, and their primary role is mechanical, serving as shock-absorbing cushions for mechanical load [9]. In mammals, the IVD is composed of a central gelatinous nucleus pulposus (NP) surrounded by an outer ring of well-arranged collagen fibres made from elastic fibrocartilage, named the annulus fibrosus (AF). Among the collagens expressed in the IVD, collagen type IX is an important component of the intervertebral disc extracellular matrix that has been repeatedly associated with the early onset of IVDD [11-13]. Collagen type IX is heterotrimeric collagen formed by the assembly of three alpha chains (a1, a2, and a3) codified by *COL9A1*, *COL9A2*, and *COL9A3* genes. Collagen type IX covalently cross-links with collagen type II, forming a macromolecular bridge between fibrils and interacting with other matrix constituents to support the stiffness and tensile strength of the tissues [14, 15]. Mutations affecting collagen IX have been linked to early onset of osteoarthritis (OA), lumbar disc disease, spinal stenosis, multiple epiphyseal dysplasia, Stickler Syndrome and ectopic mineralization of the posterior ligament [13, 16-18].

Col9a1 knockout mice show endplate degeneration with cartilage disorganisation and ectopic bone formation, suggesting a role of Col9a1 in preventing ectopic mineralization in IVDD pathology [19]. However, how mutations in *COL9A1* lead to progressive ectopic mineralization and disc degeneration remain elusive.

In teleosts, the connection of the endplates of vertebral bodies is similar in design and function to the mammalian IVD (hereafter called IVD) [20]. Centrally located vacuolated notochord cells, which have a comparable function with NP (hereafter called NP) are surrounded by a strong composite ligament that functions like the AF (hereafter called AF) [21]. The ligament is composed of, from inside to outside, collagen type II embedded in a matrix resembling cartilage, elastin and collagen type 1 fibre bundles [22]. In adult teleosts, the vacuolated notochord cells turn into a fibrous, keratinized, connective tissue (septum and notochord strand) and extracellular vacuoles [21, 23]. Recently, we have demonstrated IVDD in aged zebrafish, establishing them as a model to study disc disease [24]. Zebrafish have advantages over other organisms as they allow cell trackability using reporter lines labelling specific cell types combined with non-invasive 3D *in vivo* imaging [25, 26]. Here, we characterised IVDD and demonstrated ectopic mineralization during the lifespan of zebrafish lacking *col9a1b*. We uncovered nano structural changes associated with abnormal mineralization of the notochord in *col9a1b* mutants. We, further, used the *col9a1b* zebrafish mutant as a model to uncover mechanisms associated with ligament mineralization. Importantly, we identified and demonstrated that buffering phosphate, modulating retinoic acid, dampening fat metabolism pathways mTOR or PPaRgamma, via dietary regimen or pharmacological intervention, can reduce ameliorating ligament mineralization in *col9a1b* mutants; with bisphosphonates and calorie restriction showing the most effective reduction.

Results

Intervertebral disc ligament mineralization in zebrafish *col9a1b* mutants

We have previously demonstrated that zebrafish develop radiographic and cellular changes associated with IVDD resembling those seen in mammals [24]. Age-related degenerative changes included narrowing of the IVD space, vertebral endplate sclerosis, mineralization of the nucleus pulposus (NP) and/or annulus fibrosus (AF) with cellular and extracellular matrix disorganisation [24]. Here, we looked for signs of IVDD in adult *col9a1b* mutants using micro-computed tomography (μCT) and Alizarin Red staining. All mutants displayed fusions of the vertebral centrae throughout the vertebral column, leading to shorter fish with significantly reduced standard length **(Figure 1A, B)**. These alterations to structure were not accompanied by changes to overall BMD **(Figure 1C).** The abdominal region was consistently affected with fusions in all mutants (n=40) **(Figure 1A)**. Broadening of IVD space, osteophytosis, and sclerosis of vertebral endplates were detected even where centrae had not fused **(Figure 1A, Alizarin Red).** While we have previously reported that 80% of aged zebrafish will develop mineralization within the IVD, indicative of IVDD, in *col9a1b-/-* IVD mineralization was largely confined to intervertebral ligaments. We performed histological sections to analyse cellular aspects of degeneration in the intervertebral space and the intervertebral ligaments (NP and AF). Compromised intervertebral discs showed highly disorganised, cartilaginous, and fibrotic notochord cells in the peripheral skirts of the NP **(Figure 1E)**. Abnormal collagen was deposited within AF, and there was a reduced elastin layer suggesting events preceding disc mineralization (**Figure 1E)**. In the bone, despite no change to overall BMD, Picrosirius Red staining revealed abnormal collagen organisation within the vertebral centrae; suggestive of reduced bone quality in mutants **(Supplementary Figure 1)**.

col9a1b mutants show cellular abnormalities in the notochord epithelium cell layer

Normal vertebral column patterning with alternating vertebrae and IVDs is established by segmentation of the notochord [27]. In zebrafish, the notochord consists of vacuolated cells surrounded by an epithelial layer and a sheath layer that highly expresses collagen type IX [27]. Due to the association of collagen type IX with collagen type II [14, 15], we hypothesised that loss of *col9a1b,* would compromise the integrity of the collagen type II-based notochord sheath, leading to abnormal segmentation of the vertebral column. Additionally, Witten & Hall (2023) concluded that it is not segmented mineralization of the notochord sheath but the establishment of intervertebral spaces by the notochord, and the required thickening of the

notochord sheath, that establishes vertebral centra segmentation [20]. Thus, abnormal notochord sheath development could lead to abnormal segmentation of the vertebral column. Alizarin Red staining at stages during segmentation revealed that mutants develop the normal number of spatially distinct segments **(Figure 2A).** However, the process was delayed, and segments displayed abnormal shape with frequent clefts **(Figure 2A).** Once all segment anlagen were established (5-7 mm Standard Length-SL), there were no significant differences to centrae diameter or area (p=0.4964) **(Figure 2B)**. But mutants presented platyspondyly (widening of vertebral centrae) (p=0.0004) **(Figure 2A, C)**, a phenotype observed in the vertebral column of patients with Sticker syndrome [28]. We then measured the diameter of the notochord in the cloacal region of 5dpf larvae; mutants showed increased notochord diameter (p=0.0022) and reduced SL (p=0043) **(Figure 2D-F)**. To look for signs of cellular stress in the notochord epithelial cells, we used Tg(*col9a2:GFPCaaX*), a marker for the notochord epithelial cells, and measured cell area between chordacentrae. Mutants had higher variability of notochord epithelial cell areas, with abnormally enlarged cells, which was not accompanied by disruption notochord integrity (p=0.0317) **(Figure 2G, H)**. Cell proliferation was unaltered **(Figure 2I, J)**. No signs of oxidative stress were observed (data not shown). Our results demonstrate an important role of *col9a1b* in maintaining a normal organisation of the notochord epithelial cells, but that *col9a1b* mutants form all segments and display normal levels of notochord epithelial cell proliferation.

Structural impairment of the notochord in *col9a1b* mutants is associated with mineral deposits

We therefore postulated that a lack of *col9a1b* disrupts the properties of the notochord sheath. Immunostaining for collagen type II showed the honeycomb distribution of collagen type II, which mirrors the Col9 expressing epithelial cells, and showed increased levels in mutants **(Figure 3A)**. We also observed increased Alcian Blue staining, indicative of an alteration to glycosaminoglycan distribution throughout the notochord sheath of the mutants **(Supplementary Figure 2)**. To better understand structural changes to the notochord sheath, we sectioned samples both in transverse and sagittal planes for transmission electron microscopy (TEM). At lower magnification (3000 x), the entire diameter of the notochord can be observed in cross-section. In wt larvae, the notochord sheath is characterised by a clear delineation of the outer elastin layer, followed by the collagen type I based tube of the autocentrum that surrounds the notochord. Directly below the notochord sheath (ns), lies the cellular notochord epithelium (ne) while the notochord vacuolated cells (vc) occupy the

notochord area **(Figure 3B-D)**. In *col9a1b-/-*, the notochord sheath layer is thinner, the outer elastin layer is disrupted with clumps of poorly connected matrix visible **(Figure 3D, magenta arrowheads)**. At higher magnification (30000 x), the layers of collagen and elastin adjacent to the notochord sheath can be distinguished **(Figure 3D)**. In wt sections, the autocentrum collagen type I layers (c) can be divided into two regions with different densities. More centrally, the electron dense elastin layer (e) that surrounds the notochord sheath is clearly visible. Thick notochord sheath layer (ns) visibly composed of fibrillar collagen (type II). In mutants, this organisation is lost **(Figure 3D)**. The notochord sheath in *col9a1b-/-* shows dramatic reductions to thickness, while the elastin layer is highly disorganised or lacking. Elastin patches are also detected **(Figure 3D, cyan arrowhead)**. Our results demonstrate that *col9a1b* is required for structural integrity of the notochord sheath.

Ectopic mineralization of the intervertebral ligament is preceded by expression of *entpd5*, collagen type X, along with changes to the retinoic acid pathway, but without an altered immune response

We used Tg(*entpd5:kaeda*) as an early marker of the notochord segmentation and mineralization. Entpd5 hydrolyses extracellular nucleoside triphosphates, providing local inorganic monophosphate for biomineralization [29]. *entpd5* is segmentally expressed in the notochord sheath, which will form the mineralised chordacentra; while the interdomains will develop into IVDs [27]. *col9a1b* mutants exhibited expansion of *entpd5* expression domain, ectopically extending towards the intervertebral ligaments into the future IVDs (p=0.0317) **(Figure 4A, B)**. Using Tg(*colX:yfp)*, we detected collagen type X expression in the notochord ligaments, confirming the activation of normally expressing genes associated with chordacentrae mineralization **(Figure 4C)**. It has been previously shown that increased retinoic acid (RA) signalling during vertebral segmentation causes hyper-mineralization of the vertebral column and vertebral fusions [30]. We generated *col9a1b* mutants carrying Tg(*cyp26b1:yfp*). Cyp26 is a family of enzymes that metabolises retinoic acid, preventing its accumulation within cells and tissues, and serves as a marker for the activity of the RA signalling [31]. Ectopic expression of *cyp26b1* demonstrates activation of RA signalling which corelated with the ectopic biomineralization of mutants **(Figure 4D)**. A rupture of the notochord sheath can recruit an innate immune response and lead to an ectopic mineralization [32]. We, therefore, quantified the number of macrophages associated with the notochord epithelium cells *in vivo* using Tg(*mpeg*:mCherry) reporter line. We showed unaltered numbers of macrophages in the vertebral column of mutants **(Figure 4E, F)**. Therefore, the abnormal

cellular organisation in the notochord epithelium, does not appear to trigger an inflammatory response. Our data indicates that lack of *col9a1b* induces biomineralization of vertebral ligaments in zebrafish independent of inflammation.

Phosphate buffering prevents ectopic biomineralization of intervertebral ligaments

To explore pharmacological approaches to prevent ectopic mineralization of ligaments, we treated 15dpf *col91b* mutant larvae for ten days with either etiodronate, N,N-diethylaminobenzaldehyde (DEAB) or Ibuprofen **(Figure 4G)**. Pioneering studies from the 1960s demonstrated that extracellular inorganic pyrophosphate (PPi) could inhibit mineralization by binding to hydroxyapatite crystals, regulating mineral deposition [33]. Etiodronate is a bisphosphonate (analogous to PPi) that strongly binds to calcium phosphates, inhibiting their growth, nucleation and dissolution. Etiodronate has been used to treat heterotopic ossification, Paget's disease of bone and osteoporosis [34]. DEAB is a potent inhibitor of the enzyme retinaldehyde dehydrogenase that converts retinal to retinoic acid (RA), therefore inhibiting retinoic acid [35]. Ibuprofen is a nonsteroidal anti-inflammatory and was used to confirm ectopic mineralization in the mutants was not related to increased inflammation. We measured the length of the first ten caudal vertebral segments (separated by ligaments) from non-treated wt and *col9a1b-/-,* and *col9a1b-/-* treated with each drug (n=10 for each of the groups). Vertebral segments were measured from one IVD to the next visible IVD, such that fusion of centrae presents as increased segment length (Figure 4H). Treatment with ibuprofen did not influence the number of fusions ($p>0.99$) Fig 4H, I. Despite the overexpression of the RA pathway in mutants, DEAB only exerted a mildly protective effect ($p=0.02$), only etidronate treatment ameliorated the mutant phenotype, by reducing the number of fusion events leading to a reduction in segment length ($p=0.025$) **(Figure 4H, I, J)**. None of the treatments led to altered segment length in wild type fish (data not shown).

Transcriptomic analysis of *col9a2-/-* revealed dysregulated lipid metabolism (PPaR) and mTOR signalling pathways during development and at the onset of degeneration

Given the early onset of a phenotype in *col9a1b* mutants, they represent an ideal model to identify novel molecular mechanisms involved in and the initiation of ectopic mineralization and disc degeneration. To further identify molecular pathways involved in initiation and progression of IVDD, we performed RNAseq on *col9a1b* mutants and their unaffected siblings at 15dpf (representing initiation) and 1-year-old fish (severe pathology) from posterior larval trunk or dissected vertebral columns, respectively. We detected 868 upregulated genes and

1072 downregulated genes in larvae **(Figure 5A)**. Among differentially expressed genes (DEGs) in larvae were collagens (downregulated: *col9a1b*, *col28a2a*, *col17a1a*, *col17a1b*; upregulated: *col2a1a*, *col9a3*, *col10a1b*, *col8a1b*), matrix proteins (*matn1a*, *tnc*, *krt4*, *krt93)* **(*Supplementary Table 1*)**. Gene set enrichment analysis (GSEA) of larvae transcriptome showed enrichment for genes associated with extracellular matrix receptor interaction and focal adhesion **(Figure 5B, C)**. However, there were also many non-matrix related pathways; among those which were highly enriched were pathways associated with glycolysis, retinol metabolism and PPAR signalling pathway (lipid metabolism) (KEGG). From dissected adult vertebral columns, we detected 319 and 249 genes up and downregulated, respectively **(Figure 5D, *Supplementary Table 1*)**. Only 99 genes were differentially expressed both in larvae and in adults, including *col9a1b*, *matn1a*, *wnt4b* and *col8a1b* **(*Supplementary Table 1*)**. Among extracellular matrix and focal adhesion genes, GSEA pointed to the involvement of mTOR and p53 signalling pathways, oxidative phosphorylation, extracellular interaction, and cell cycle (KEGG) **(Figure 5E, F)**. A few randomly selected genes from the highly DEG set (**Table 1 and Table 2)** were validated using qPCR **(Figure 5G)**. Our data suggest that lipid metabolism PPaR and mTOR signalling pathways are involved in ligament mineralization and disc degeneration.

Dampening lipid metabolism systemically reduces vertebral column fusions in *col9a1b* mutants

Given the indication of altered lipid metabolism, we used Nile Red staining in live fish to observe adipose tissue at 15 and 30 dpf. Surprisingly, *col9a1b-/-* exhibited increased fat, quantified through the measurement of visceral adipocyte droplet areas **(Figure 6A, B)**. Nile red staining also colocalised with regions of ectopic mineralization in the intervertebral ligaments as observed by Tg(*Entpd5:kaeda*) **(Figure 6C)**. Taken together with the RNAseq data, these data suggest that there is an association between altered fat metabolism and ectopic mineralization. To explore this relationship further, we limited adipogenesis by caloric restriction **(Figure 6D)**. This regimen involved minimal feeding, with fish being fed only once every three days for two weeks, beginning at 15dpf. The regimen led to a dramatic reduction to area of visceral adipose tissue **(Figure 6E, F).** The caloric restriction in wild type fish also led to changes in the vertebral column of wild type controls, where the vertebrae became broader with reduced mineralization **(Figure 6E, asterisks)**. Importantly, the number of vertebral fusion events in *col9a1b-/-* was reduced **(Figure 6E, G)**. Feeding restriction can impact multiple pathways, so to more directly test the association with PPRagamma and mTOR

we inhibited PPaRgamma and mTOR using GW9662 a potent antagonist of PPARgamma [36], and rapamycin, an inhibitor of mTOR [37] **(Figure 6H, I)**. GW9662 significantly reduced visceral fat area in control and mutants. Rapamycin reduced visceral fat area in both groups, but this was only statistically significant in the mutants **(Figure 6I, K)**. Treatment with GW9662 and mTOR reduced the numbers of vertebral fusions in mutants, albeit more dramatically in the rapamycin treated group. Our data suggests that targeting lipid metabolism through PPARgamma and mTOR pathways systemically can reduce ectopic intervertebral ligament mineralization in vivo, during early stages of mineralization.

Discussion

Although collagen type IX is associated with intervertebral disc disease and ligament mineralization, the specific mechanisms underlying its role in these pathologies have not previously been defined. Here, we studied the early events during initiation of disc mineralization and degeneration, in *col9a1b* mutants. Our data suggest that pathogenesis is preceded by structural changes to the matrix rich notochord sheath, which lead to altered initiation of mineralization, but that progression can be modulated by altering phosphate nucleation or by disruption of lipid metabolism.

Collagen type IX functions as a macromolecular bridge between fibrils and other matrix components, contributing to the cohesive and compressive properties of cartilaginous tissues [38]. Here, we present evidence supporting the role of collagen type IX in maintaining the structural integrity of intervertebral disc ligaments. In *col9a1b* zebrafish mutants, premature IVDD was observed. This degeneration primarily affected the outer layer of the intervertebral disc (IVD). This phenotype aligns with findings in knockout mice, which also show fissures in the annulus fibrosus and disorganized collagen [19, 39]. We detected structural changes in vertebral ligaments during development, including abnormal deposition of collagen type II and the accumulation of mineral crystals. These changes ultimately led to vertebral fusions in adult zebrafish. Our findings corroborate the well-established role of collagen type IX as an adaptor between the collagen network and the extracellular matrix [14, 15]. This role is crucial for the proper organization of collagen types I and II, as well as elastin, within the notochord sheath. The absence of *col9a1b* led to differential expression of other extracellular matrix components known to interact with collagen type IX, such as matrilins [40], along with other proteins like *col8a1b* and *wnt4b*, which are important for notochord sheath homeostasis [41, 42]. Interestingly, like *col9a1b*-/- mutants, *col8a1a*-/- mutants exhibit notochord bending, which eventually leads to vertebral fusions in adults [41]. Additionally, medaka *wnt4b*-/- mutants show ectopic mineralization in the vertebral ligaments, resulting in similar fusions [42]. Our results suggest a direct or indirect effect of col9 in *col8a1a* and *wnt4* in disc ligaments, and also highlight that damage to the notochord sheath often results in vertebral fusions, as previously demonstrated in models of notochord injury and scarring [32, 43].

Our findings support the essential role of collagen type IX in maintaining not only the structural integrity of the notochord sheath but its biomechanics. In mice, the lack of collagen type IX resulted in disorganized collagen networks, leading to alterations in the biomechanical

properties of the extracellular matrix, softening it [44]. The zebrafish notochord, which experiences high mechanical stress due to the growth-related increase in the number and volume of vacuolated notochord cells [45], becomes particularly vulnerable. In mutants a softened or thinner notochord sheath inflation of the notochord could be facilitated, resulting in the observed notochord widening. Altered biomechanics of the notochord and its sheath likely positively impact mineralization.

Here we establish *col9a2-/-* zebrafish model as an effective system for studying ectopic mineralization within vertebral ligaments. Although zebrafish lack endochondral endplates, precluding a direct comparison with the vertebral endplates of mammals like mice, this distinction enables us to differentiate and isolate the mechanisms underlying ectopic mineralization in ligaments from those involved in endochondral ossification. Our study revealed a significant role for phosphate nucleation, evidenced by increased *entpd5* expression in notochord sheath cells, alongside retinoic acid (RA) signalling, marked by increased expression of *cyp26b1* during the mineralization process. Importantly, this process is also associated with elevated expression of the mineralization marker *col10a1* and does not appear to activate an innate immune response. Transcriptomic analysis also showed upregulation of mineralization marker, *col10a1*, and dysregulation of retinoic acid pathway. Although inhibition of retinoic acid pathway reduced vertebral fusion in our *col9a1b* mutant, it did not fully prevent fusions. On the contrary, modulation of phosphates showed a higher impact in controlling ectopic mineralization. Our experiments did not support a role for inflammation in the initiation of mineralization in this mutant line.

Historically, Fleisch et al. (1960s) discovered that extracellular inorganic pyrophosphate serves as a critical inhibitor of bio-mineralization [44], as it counteracts the ability of calcium and inorganic phosphate to crystallize into hydroxyapatite. In this context, *enpp1* (ectonucleotide pyrophosphatase/phosphodiesterase) locally provides pyrophosphate while *entpd5* hydrolyses extracellular nucleotide diphosphates into nucleotide monophosphates and inorganic phosphate. Loss-of-function mutations in *enpp1* and *entpd5* show opposing effects, with mutation of enpp1 resulting in ectopic mineralization in the notochord sheath, resembling that seen in *col9a1b-/-*, whereas loss of entpd5 lead to an absence of mineralization [29]. Correspondingly, treatment with the bisphosphonate etidronate effectively reduced vertebral fusions. Indeed, a novel approach in the field of hereditary ectopic mineralization disorders is treatment with bisphosphonates. It has been shown to reduce arterial wall

mineralization [46], and has been approved to treat heterotopic mineralization, including fibrodysplasia ossificans progressiva [47]. Bisphosphonates are also well-known treatments for osteoporosis, a disease characterised by bone loss, where they act as powerful inhibitors of bone resorption [48].

Our transcriptomic analysis revealed dysregulation of lipid metabolism and mTOR signalling pathways in *col9a1b* mutants. These findings were supported by increased adipose tissue observed in mutants, linking altered lipid metabolism to ligament mineralization and vertebral fusion. Although lipid metabolism disorder has an important impact in disc disease development, the specific involved mechanisms remain undetermined as it may contribute to disc disease through inducing oxidative stress, activating endoplasmic reticulum stress, inducing extracellular matrix degradation, cell apoptosis, or mediating autophagy [49] . Obesity has also been independently associated with ligament mineralization [50] . Although *COL9A2* has not yet been associated with obesity, a methylation study comparing 20 obese and 11 normal weight children (age 8.56 ± 1.34) identified *COL9A3*, suggesting undetermined role of collagen type IX in obesity [51]. Interestingly, we found that *col9a2* mutants had increased visceral fat, and by subjecting mutants to dietary restriction we demonstrated that caloric restriction reduced vertebral fusions in line with the reduction to adipose tissue, likely implicating trans metabolic changes in the pathological process of ligament mineralization. Pharmacological inhibition of PPARγ and mTOR pathways reduced fat content and ameliorated vertebral fusion in our fish, highlighting different potential angles to tackle disc mineralization. However, pharmacological treatments did not completely inhibit mineralization as seen with dietary restriction. Because phosphate also largely comes from food intake, dietary restriction would also reduce available phosphate for mineralization, and indeed dietary restriction partially phenocopies bisphosphonate treatment. While our mutants develop IVDD phenotypes which resemble those seen in aged fish, the early developmental onset might mean that mechanisms that lead to initiation and progression may differ between those seen in severe monogenic spondylosis and naturally occurring later degenerative events. Therefore, further studies are necessary to test whether these pathways can prevent disease progression in naturally aged zebrafish.

In conclusion, our study establishes *col9a1b* mutants as a robust model for studying IVDD and ectopic mineralization, demonstrating key roles for phosphate metabolism, retinoic acid signalling, and lipid metabolism in the pathogenesis of ligament mineralization. These insights contribute to the broader understanding of disc degeneration and offer potential

therapeutic strategies aimed at targeting phosphate buffering, lipid metabolism, and mTOR signalling to prevent or mitigate disease progression.

Material and Methods

Zebrafish husbandry and lines

Zebrafish were raised and maintained under standard conditions [56]. Animal experiments were ethically approved by the University of Bristol Animal Welfare and Ethical Review Body (AWERB) and conducted under UK Home Office project license. *Col9a1b*^{sa12182} was generated through the Zebrafish mutation project by the Sanger Institute and acquired through the European Zebrafish Resource Centre. Mutants carry an A>T mutation in an essential splice site in the second exon, affecting 525 amino acids out of the total 681. The mutants are expected to be null mutants. Mutants survive to adulthood and are fertile. Tg(*cyp26*b1:YFP) [57], Tg(*col9a2:GFPCaaX*)[58], Tg(*entpd5*:kaeda) [30], Tg(*mpeg1*:mCherry) [59], Tg(*col10a1aBAC:citrine*)[60].

Micro-Computed Tomography (µCT)

Male adult fish (1 year old) were fixed in 4% PFA for 1 week followed by sequential dehydration to 70% ethanol. Fish were scanned using an XT H 225ST micro-CT scanner (Nikon) with 21 voxel size of 21 µm and 5 µm for detailed geometric analysis, using an x-ray source of 130 kV, 53 µA and without additional filters. Images were reconstructed using CT Pro 3D software (Nikon). Amira 6.0 was used for image analysis and to generate 3D volume and surface renders. For calculations of tissue mineral density (TMD) defined as measurement restricted to within the volume of calcified bone tissue [52], the first three caudal vertebrae centra (C1, C2 and C3) were segmented and mean grey values were retrieved. Grey values were calibrated with phantoms of known densities (0.25 and 0.75 g.cm^3 of CaHA), and used for density calculations, as previously described [52]. Amira (6.0) was used for picture acquisition and fish standard length (SL) measurements.

Histology

Adult fish were decalcified in 1M EDTA solution for 20 days at room temperature (n= 3 per group). Samples were dehydrated to ethanol, embedded in paraffin and sagittal sections at 8 µm thickness taken through the entire vertebral column. Slides were de-waxed and stained sequentially every third slide with either Toluidine Blue [53] and every other with Picrosirius red [54]. Acid Fuchsin Orange G (AFOG) staining was performed in selected slides as previously described [55]. Images were acquired on a Leica DMI600 inverted microscope, using 20X and 40X oil objectives, LAS software, and a DFC420C colour camera for Toluidine Blue stained sections, polarising filter was used for pictures of the

Picrosirius Red stained sections. Quantification of mean pixel values from slides stained with Picrosirius Red were performed in Fiji[66].

Alizarin Red Staining

Alizarin Red S staining was performed using standard protocols [56]. Images were acquired on Zeiss Stemi 305 (1.2 Megapixel Wifi camera). Live Alizarin Red S staining was carried out as previously described [57]. Images were acquired laterally using a Leica MZ10F, with DFC7000 T camera.

Vertebral measurements

Segments were measured from 3-weeks-old fish vertebral column undergone Alizarin Red Staining. Centrae areas and their middle height were calculated from the first five centra at the caudal region of the vertebral column. Cell areas were measured at the intervertebral disc regions of 15dpf Tg(*col9a2:GFPCaaX*). Measurements were performed using Fiji[58]. For volumetric analysis of *entpd5* expression, we used Amira (FEI) to segment three centra from each fish (n=5) and quantify the number of pixels within the volume.

Immunohistochemistry

Standard protocols were used for immunostaining. Anti-Collagen II (1:500, DSHB) was used as primary antibodies and Dylite 488 goat anti-mouse IgG and Dylite 550 goat anti-rabbit IgG (1:1000, Molecular Probes) as secondaries. Images were taken using a Leica DMI6000 inverted epifluorescence microscope using a 20X dry lenses and Leica DFC365FX as the camera.

Confocal imaging

Larvae were anesthetized in MS222 and mounted laterally in 1% low-melting-point agarose. Images were carried out using a Leica TCS SP8 AOBS confocal laser scanning microscope attached to a Leica DMi8 inverted epifluorescence microscope using 10x dry lens Image acquisition was performed using LASX software.

Transmission Electron Microscopy (TEM)

Larvae were fixed for 24 h in 2.5% PFA, 1.5% glutaraldehyde, 0.1 M sodium cacodylate buffer (pH 7.4) and 0.001% $CaCl_2$ at 4 °C. Specimens were subsequently rinsed in 0.1 M sodium

cacodylate buffer with 10% saccharose and then post-fixed for 2 h in 1% OsO_4 solution in 0.1 M cacodylate buffer containing 3% saccharose. The samples were then dehydrated in a series of graded ethanol solutions and embedded in epon epoxide medium [59]. Semi-thin 1 μm sections were cut on a Microm HM360 microtome (Marshall Scientific, Hampton, NH, USA), stained with toluidine blue at pH 9 for 2 min (0.5% toluidine blue, 1% $Na_2B_4O_7$ in dH_2O), rinsed with H_2O and mounted with DPX. For transmission electron microscopy (TEM) analysis, ultrathin sections (about 70 nm) of the region of interest were prepared on an UltracutE ultramicrotome (Reichert-Jung, Buffalo, NY, USA), contrasted with uranyl acetate and lead citrate [60], analysed with a Jeol JEM 1010 transmission electron microscope (Jeol Ltd., Tokyo, Japan) operating at 60 kV. Microphotographs were taken with a Veleta camera (Emsis, Muenster, Germany).

Cell Proliferation (Edu)

Cell proliferation was assessed using the Click-iT EdU imaging kit (Invitrogen, C10337), according to the manufacturer's instructions. Briefly, larvae at 4dpf were treated with 400 μM EdU in Danieaus for 24 hours. Larvae were fixed in 4% PFA at 4°C overnight, permeabilised in 20 mg/ml proteinase K, then incubated in the Click-iT reaction cocktail for 30 min. Larvae were immunostained for collagen type II and co-stained with DAPI. Confocal images were taken laterally using a 20x objective at 2.5x zoom. Images were analysed using LAS-X (Leica). EdU+ cells within the notochord sheath region through confocal z stacks correspondent to the notochord only.

Oxidative Stress

Visualization of reactive oxygen species (ROS) was performed using the probe chloromethyl-2′,7′-dihydrodichlorofuorescein diacetate (CM-H2DCFA) as a nonfuorescent cell-permeative compound. Once in the intracellular environment, esterases cleave the acetate groups of the nonfluorescent dye 2′,7′-dichlorofuorescein (DCF). DCF retained intracellularly is oxidized by intracellular ROS and becomes fluorescent. 15dpf larvae were incubated with 10μM CM-H2DCFA for 60 min, followed by washes in Danieaus to remove excess of dye and visualisation under a fluorescent stereomicroscope.

Drug Treatments

Zebrafish were raised to 15 dpf. Groups of 10 fish of similar standard lengths were placed in small tanks (500ml) containing 100-200 mL of drug solution, replaced every 48h, and protected from light. Diethylaminobenzaldehyde (DEAB)(10µM) (Alfa Aesar, A11825)[30], ibuprofen (10µM) (Sigma, I4883), etiodronate (100µM) (Sigma, P5248) [61], GW9662 (100nM) (Stratech Scientific, S2915) [62] or DMSO (0.01%). Higher concentrations of GW9662 were tested and were lethal. Fish were fed with brine shrimp once daily.

Feeding regime for caloric restriction

col9a1b mutants and wt were raised to 15dpf. Groups of 20 fish of similar standard lengths were placed in tanks of 6L. Fed fish were fed twice daily with brine shrimp, and once with dry food. Fish undergone caloric restriction, were fed with brine shrimp once every three days. After 3 weeks of the feeding schedule, the fish were culled and fixed in 4% PFA.

Live Nile Red Staining

Sock solution of Nile Red (ThermoFisher) was prepared in acetone to a final concentration of 1.25 mg/mL. Fish were incubated for 5 min in a working Nile Red solution diluted in Danieaus to 0.5 µg/mL and washed in Daniaus prior to imaging. Images were acquired laterally using a Leica MZ10F, with DFC7000 T camera and Red Channel. Quantification of fat deposits was performed in FIJI using Nile Red positive areas and additional correction by fish standard length.

RNAseq

col9a1b-/- and wt 15dpf larvae had their posterior axis (tail portion) dissected and pooled (n=20) for RNA extraction. Experiments were performed from triplicated of pools (3 pools (n=20) for each group). Total RNAs were extracted using TRIzol Reagent (Life Technologies) and purified using RNeasy MinElute Cleanup Kit (Qiagen). The concentration and quality of RNAs were evaluated by NanoDrop 2000 (Thermo Scientific), RNA screenTape (Agilent Technologies), and Agilent Bioanalyser 2100. Samples with RNA integrity (RIN) values >8 were submitted for sequencing. cDNA library preparation, sequencing, and basic bioinformatics were performed by Novogene (polyA enrichment, Illumina NovaSeq 6000, Pair-end 150, 15Gb raw data per sample). Reads were aligned to the zebrafish reference genome GRCz11 (Genome Reference Consortium Zebrafish Build 11), INSDC Assembly GCA_000002035.4. Differential expression analysis and Enrichment analysis (Gene Ontology, GO, and Kyoto Encyclopedia of Genes and Genomes, KEGG).

qPCR

Total RNA from Zebrafish was extracted using Trizol. RNA was reverse transcribed into cDNA using SuperScript™ IV Reverse Transcriptase (Thermofisher) and random hexamers. The mRNA levels were determined by reverse transcription quantitative PCR (RT-qPCR) using SYBR green dye on Applied Biosystems Quantstudio3 PCR cycler (Thermo). Primers were validated with dissociation curves. The expression of genes was normalized to *eef1α.* The following primers were used: eef1a-F GTGGTATCACCATTGACATTGC, eef1a-R TCAGCCTGAGAAGTACCAGTGA; col9a1b-F CAGACAAGTGTGCATGCGAG; col9a1b-R AAACCACTGTCACCTTGGGG; wnt4b-F GTAGACCAAGTCCCGTGTGG; wnt4b-R CGGTGCAGTGCTGAAAGAAC; otomp-F AAGCTCTTGTGTCCTGACGG; otomp-R TCCTCCAAACGCACTACCAC; epx-F ATTTGCATCCTGGAGGGTGG; epx-R CCTCCCTGAGCCTGGAAAAG; cyp2ae1-F GCAGGAGTGTCGCTTTCTCT; cyp2ae1-R TCGTACTCAAAGCGGTGACC; lamtor5-F GCAGGCTGCTTCTCTAACCA; lamtor5-R TGCCATCTTATGCACAGCCA; fbxo43-F CACACTCAGAGCAGAGCACA; fbxo43-R CACCGGCTCTGATACGACTC.

Acknowledgements

EK and BLP is funded by Versus Arthritis (Career Development Award, 23115). We thank the Histology facility and Wolfson Bioimaging facility of the University of Bristol for their support and service.

Conflicts of interest

We declare no competing interests.

Author contributions

The project was conceived and designed by EK. EK performed most experiments, BLP performed Alizarin Red and quantifications. JM performed cell proliferation assay, RR performed RTPCR. EK drafted the manuscript. All authors contributed to editing the manuscript.

Data availability

Raw and processed data generated in this study will be available via a DOI at data.bris upon article acceptance.

Figure legends

Figure 1. Vertebral fusions in zebrafish *col9a1b* mutants. A) μCT of adult zebrafish. Higher resolution images are presented on the right panel to show vertebral fusions (dashed green lines). Endplate sclerosis (yellow arrowhead); IVD mineralization (magenta arrowhead). Scale bars= 1mm. B) Standard fish length (wt n=11; *col9a1b-/-* n=8). C) Cortical bone mineral density (BMD) (wt n=5; *col9a1b-/-* n=5). Nonparametric T-tests and Mann-Whitney test (B and C). All significant p values are as indicated. D) Schematic of a histological section of the vertebral column of zebrafish not at the middle plane showing two consecutive IVDs. IVD = intervertebral disc; NP = nucleus pulposus; AF = annulus fibrosus; co = collagen layers; el = elastin layer; b = bone; ns = notochord sheath. E) Histological sections of zebrafish IVDs stained with Toluidine blue or AFOG. Black arrow (fibrosis), magenta arrowheads (abnormal collagen layer), black arrowhead (abnormal cartilage trapped in the NP). Scale Bars= 50um.

Figure 2. Vertebral fusions are preceded by ectopic expression of mineralization markers during vertebral segmentation. A) Live alizarin red of same SL wt and *col9a1-/-*. Higher magnification of same vertebral regions (magenta dashed box) is shown. Note all vertebral segments formed in the wt and delayed formation in *col9a1b-/-* (cyan dashed lines). Scale bars are indicated. B) Centrae areas (wt n= 9; *col9a1b-/-* n= 6). C) Middle height of centrae (wt n= 9; *col9a1b-/-* n= 6). D) Transmitted light image of 5dpf larvae. higher. Magnification of the notochord region is hown on the right panel. E) Notochord diameter. F) Larvae SL (standard length). G) 15dpf wt and *col9a1b-/-* with notochord sheath epithelium labelled with Tg(*col9a2:GFPcaaX*) and live stained with Alizarin Red. Higher magnification shown in the right panel. White arrowhead (ectopic mineralization), blue arrowhead (higher shape distortion in the middle of chordacentrae), white dashed lines (notochord sheath cell perimeters). H) Cell areas of the notochord epithelium of wt (n=5) and *col9a1b-/-* (n=5). I) Cell proliferation assessed through EdU labelling. J) Quantification of EdU+ cells in the notochord region. Nonparametric T-tests and Mann-Whitney test, p value is annotated.

Figure 3. Lack of *col9a1b* causes structural impairment of the notochord sheath. A) Immunofluorescence for collagen type II in 5dpf larvae. Note higher signal adjacent to notochord epithelium cells (arrowheads). Higher magnification of mutant notochord is shown on the right panel, to highlight positioning of each notochord epithelium cell through Tg(*col9a1:gfp)* overlapped with immunostaining for collagen type II. Arrows point to the edge

of notochord epithelium cell, showing increased deposition of collagen type II. Scale bars = 50µm. B) Diagram of a cross section through the notochord. The notochord is formed by the notochord sheath (ns), notochord epithelium (ne) and vacuolated cells. C) Diagram of a region of the notochord (dashed square in B) in higher magnification. From the outside to the inside of the notochord, we detect the collagen type I layer (c), the elastin layer (e), the notochord sheath (ns) and the epithelium layer (e). D) TEM of cross sections and sagittal sections of the wt and *col9a1b-/-* notochords. Scale bars are indicated in each picture.

Figure 4. *col9a1b* is important to maintain cellular integrity within the notochord sheath epithelium. A) 15dpf wt and *col9a1b-/-* carrying Tg(*entpd5:kaeda*) and live stained with Alizarin Red (mineralised bones). Note ectopic expression of *entpd5* in chordoblasts (arrowhead) within the IVD region. B) Quantification of volume occupied by *entpd5* positive cells of the notochord epithelium of wt (n=5) and *col9a1b-/-* (n=5). Nonparametric T-tests and Mann-Whitney test, p value is annotated. C) 15dpf wt and col9a1b-/- carrying Tg*(colX:yfp*) (mineralization marker) and Tg(*col2:mCerry*) Noce ectopic expression of colX in chordoblasts within the IVD (arrowhead). D) 15dpf wt and col9a1b-/- carrying Tg(*cyp26b1:yfp*) (retinoic signalling pathway,) and live stained with Alizarin Red (mineralised bones). Note ectopic expression of *cyp26 (*arrowheads*)*. E) 21 dpf wt and *col9a1b-/-* with macrophages labelled through Tg(*mpeg:mCherry*). Macrophages were counted within ten centrae (five centrae indication with magenta dashed box). F) Macrophage numbers in centrae of wt (n=9) and *col9a1b-/-* (n=7). G) Representative schematics of drug treatment (Etiodronate (100µm), Diethylaminobenzaldehyde (DEAB)(10µM) and ibuprofen (10µM). Drug treatment started at 15dpf and finished at 30dpf. Drug solution was refreshed every 48h. Fish were culled and fixed at 3dpf followed by Alizarin Red Staining and imaging. H) Images of wt and drug treated fish at 30dpf stained with Alizarin Red S. I) Fusions of the caudal vertebral segments were detected through measurement of length of the segments. J) Graph showing segment lengths and respective drug treatments. (B, F) Nonparametric T-tests and Mann-Whitney test, all significant p values are as indicated. (J) Non-parametric ANOVA, Kruskal-Wallis, Dunn's multiple comparisons test (*p<0.5; **p<0.05; ***p<0.005). Scale bars = 50µm.

Figure 5. Transcriptomic analysis suggests lipid metabolism and mTOR pathways in ectopic mineralization of *col9a1b-/-*. A) Volcano plot showing differentially up (green dots) and down (red dots) regulated genes between wt and *col9a1b-/-* at 15 dpf. B) Gene ontology (GO) enrichment analysis of biological processes differentially expressed genes (DEGs)

between wt and *col9a1b*-/- at 15 dpf. C) Kyoto Encyclopedia of Genes and Genomes (KEGG) pathway enrichment analysis of differentially expressed genes (DEGs) between wt and *col9a1b*-/- at 15 dpf. D) Volcano plot showing differentially up (green dots) and down (red dots) regulated genes between wt and *col9a1b*-/- at 1 year-old. E) Gene ontology (GO) enrichment analysis of biological processes differentially expressed genes (DEGs) between wt and *col9a1b*-/- at 1 year-old. F) Kyoto Encyclopaedia of Genes and Genomes (KEGG) pathway enrichment analysis of differentially expressed genes (DEGs) between wt and *col9a1b*-/- at 1 year-old. G) qPCR for some of the up-down regulated genes at 15dpf and 1 year-old. Unpaired t-test was used. Numbers of samples are as displayed in the graphs.

Figure 6. Modulating fat in *col9a1b-/-* partially ameliorates ligament ectopic mineralization. A) Nile Red staining lipids in wt and *col9a1b-/-* at 15dpf and 30dpf. Visceral fat was quantified by drawing around the fat area and quantifying pixel numbers. B) Graph of quantification of visceral fat at 15dpf and 30 dpf (1mpf). C) wt and col9a1b carrying Tg(entpd5:kaeda) and live stained with Nile Red. Note fat droplets around the vertebral column in mutants. D) Schematics illustrating dietary regimen starting at 15dpf and ending at 30dpf, followed by live Nile Red Red Staining and ex-vivo Alizarin Red staining. E) wt and *col9a1b*-/- stained with Nile Red and Alizarin Red Staining at 30dpf. Asterisks in wt undergone dietary restriction, and Alizarin Red, show less mineralised centrae. Magenta asterisks in col9a1b normal diet, alizarin red, point to fused vertebral centrae. F) Graph of quantification of visceral fat area in wt and col9a1b-/- under normal and dietary restriction regimen. G) Quantification of vertebral centrae fusions in the caudal region at 30dpf, after dietary regimen. H) Schematics illustrating drug treatment (GW9662) and Rapamycin starting at 15dpf and ending at 30dpf, followed by live Nile Red Red Staining and ex-vivo Alizarin Red staining. I) wt and *col9a1b*-/- stained with Nile Red and Alizarin Red Staining at 30dpf. Magenta asterisks in *col9a1b* DMSO, alizarin red, point to fused vertebral centrae. J) Graph of quantification of visceral fat area in wt and *col9a1b-/-* subjected to respective drug treatment. K) Quantification of vertebral centrae fusions in the caudal region at 30dpf, after drug treatment. Scale bars = 100µm. (B, G) Mann-Whitney test. (F,J) Non-parametric ANOVA with Kruskal-Wallis test. (K) Ordinary one-way ANOVA. (*p<0.5; **p<0.05; ***p<0.005; **** p<0.0005)

Tables

Table 1. Top genes up and downregulated in larvae (15dpf)

GENE_NAME	GENE_DESCRIPTION	LOG2FOLDCHANGE	PVALUE	PADJ
RIDA	reactive intermediate imine deaminase A homolog	-8.5886013	1.95E-23	2.69E-21
STK3	serine/threonine kinase 3 (STE20 homolog, yeast)	-8.1049639	5.15E-33	1.24E-30
CNOT6L	CCR4-NOT transcription complex, subunit 6-like	-7.7479189	4.31E-83	6.75E-80
TDO2A	tryptophan 2,3-dioxygenase a	-7.3293217	1.56E-44	6.95E-42
TMEM106BB	transmembrane protein 106Bb	-7.1918423	8.29E-25	1.20E-22
CHRNE	cholinergic receptor, nicotinic, epsilon	-6.7893907	5.88E-56	3.90E-53
VAMP8	vesicle-associated membrane protein 8 (endobrevin)	-6.7799593	2.33E-21	2.67E-19
AKAP12B	A kinase (PRKA) anchor protein 12b	-6.4934245	8.35E-159	3.66E-155
EIF2AK3	eukaryotic translation initiation factor 2-alpha kinase 3	-6.4197676	1.26E-28	2.36E-26
TUFT1A	tuftelin 1a	-6.4112533	2.32E-168	1.27E-164
NT5C1AA	5'-nucleotidase, cytosolic Iaa	-6.2147133	7.09E-70	7.77E-67
NPDC1B	neural proliferation, differentiation and control, 1b	-6.1310121	1.76E-18	1.51E-16
ARL4AB	ADP-ribosylation factor-like 4ab	-6.1065339	2.45E-36	7.68E-34
NRARPA	NOTCH regulated ankyrin repeat protein a	-6.04002	7.35E-44	3.10E-41
SCIN	scinderin	-6.0159254	5.31E-26	8.49E-24
TNC	tenascin C	-5.9862506	6.21E-62	5.67E-59
ANTXR2A	anthrax toxin receptor 2a	-5.95687	1.70E-20	1.83E-18
RPIA	ribose 5-phosphate isomerase A (ribose 5-phosphate epimerase)	-5.7528145	9.41E-43	3.89E-40
HKDC1	hexokinase domain containing 1	-5.6346676	4.02E-22	4.97E-20
IGSF9A	immunoglobulin superfamily, member 9a	-5.449408	5.22E-26	8.40E-24
MROH1	maestro heat-like repeat family member 1	-5.037326	2.20E-34	6.24E-32
PVALB7	parvalbumin 7	-4.8664851	4.52E-207	9.90E-203
ATP6V1B2	ATPase H+ transporting V1 subunit B2	-4.553207	1.92E-26	3.13E-24
HSD11B1LA	hydroxysteroid (11-beta) dehydrogenase 1-like a	-4.5337081	1.05E-30	2.31E-28
MHC1ZFA	major histocompatibility complex class I ZFA	-4.3039176	7.22E-22	8.74E-20
ABCG2B	ATP-binding cassette, sub-family G (WHITE), member 2b	-4.286831	1.21E-25	1.86E-23
CHD4B	chromodomain helicase DNA binding protein 4b	-3.9681154	1.29E-70	1.48E-67
COL9A1B	collagen, type IX, alpha 1b	-3.792603	4.53E-58	3.42E-55
KLF2A	Kruppel-like factor 2a	-3.7318737	1.11E-24	1.59E-22
ATXN1A	ataxin 1a	-3.7027879	3.48E-28	6.35E-26
RIPOR2	RHO family interacting cell polarization regulator 2	-3.6396471	1.46E-27	2.59E-25
EMC2	ER membrane protein complex subunit 2	2.35596554	3.72E-23	4.97E-21
TXNDC9	thioredoxin domain containing 9	2.46653388	1.87E-45	9.11E-43
RAB41	RAB41, member RAS oncogene family	2.5193345	1.58E-31	3.61E-29
GAMT	guanidinoacetate N-methyltransferase	2.62956521	2.16E-61	1.89E-58
AGK	acylglycerol kinase	2.64857108	6.26E-28	1.13E-25
SLC4A1A	solute carrier family 4 (anion exchanger), member 1a (Diego blood group)	2.66499403	3.92E-80	5.72E-77
MHC1UBA	major histocompatibility complex class I UBA	2.69089894	5.13E-35	1.50E-32
SLC34A1A	solute carrier family 34 (type II sodium/phosphate cotransporter), member 1a	2.71308167	2.33E-36	7.41E-34
PPP1R8B	protein phosphatase 1, regulatory subunit 8b	2.7182423	4.58E-20	4.60E-18
MATN1	matrilin 1	2.80242744	6.91E-132	2.16E-128
MB	myoglobin	2.84008015	1.70E-104	3.73E-101
ISG20	interferon stimulated exonuclease gene	2.89735413	6.19E-26	9.82E-24
TGM2L	transglutaminase 2, like	2.96605327	2.55E-20	2.68E-18
TMEM204	transmembrane protein 204	3.01072715	5.08E-18	4.26E-16
IER5	immediate early response 5	3.0753967	1.02E-21	1.20E-19
TMEM177	transmembrane protein 177	3.17973181	2.34E-20	2.48E-18
HSPA8	heat shock protein 8	3.37514473	4.41E-169	3.22E-165
OTOS	otospiralin	3.46391183	1.53E-29	2.99E-27
LONRF1	LON peptidase N-terminal domain and ring finger 1	3.48242957	2.13E-47	1.14E-44
BCAM	basal cell adhesion molecule (Lutheran blood group)	3.4837439	2.33E-28	4.32E-26
PA2G4B	proliferation-associated 2G4, b	3.5878932	3.50E-118	9.59E-115
CTCF	CCCTC-binding factor (zinc finger protein)	3.88014695	6.62E-28	1.19E-25
ACTC1A	actin, alpha, cardiac muscle 1a	3.90862444	1.05E-83	1.76E-80
COCH	coagulation factor C homolog, cochlin (Limulus polyphemus)	4.34428843	7.92E-186	8.67E-182
RIPOR1	RHO family interacting cell polarization regulator 1	4.46923816	3.59E-18	3.04E-16
KNL1	kinetochore scaffold 1	4.53141403	1.45E-36	4.66E-34
C3A.2	complement component c3a, duplicate 2	4.66390337	2.75E-24	3.89E-22
TNNI2A.1	troponin I type 2a (skeletal, fast), tandem duplicate 1	4.91540404	3.11E-30	6.48E-28
OTOMP	otolith matrix protein	5.44296107	7.23E-30	1.45E-27
EPX	eosinophil peroxidase	6.4718253	1.11E-18	9.66E-17

Table 2. Genes up and down regulated in adults (1 year old).

GENE_NAME	GENE_DESCRIPTION	LOG2FOLDCHANGE	PVALUE	PADJ
PFKMB	phosphofructokinase, muscle b	-4.114844	8.31E-08	2.26E-05
KDM5BA	lysine (K)-specific demethylase 5Ba	-4.2049432	1.68E-26	6.09E-23
MXB	myxovirus (influenza) resistance B	-4.3118799	1.41E-07	3.64E-05
EHMT1B	euchromatic histone-lysine N-methyltransferase 1b	-4.3876646	4.60E-21	1.00E-17
NLRC8	NLR family CARD domain containing 8	-4.4859516	1.75E-22	5.44E-19
CYP2AE1	cytochrome P450, family 2, subfamily AE, polypeptide 1	-5.3157081	1.87E-09	8.49E-07
OLFML3B	olfactomedin-like 3b	-5.5230509	1.30E-45	1.41E-41
VPS37A	vacuolar protein sorting 37A	-5.5928272	4.73E-08	1.49E-05
CCDC88AA	coiled-coil domain containing 88Aa	-5.6489702	2.57E-07	6.08E-05
IFIT8	interferon-induced protein with tetratricopeptide repeats 8	-5.7037997	2.83E-10	1.66E-07
LAMTOR5	late endosomal/lysosomal adaptor, MAPK and MTOR activator 5	-6.3165675	9.60E-11	6.33E-08
VWA10.1	von Willebrand factor A domain containing 10, tandem duplicate 1	-6.3799126	2.62E-08	9.21E-06
MTUS1B	microtubule associated tumor suppressor 1b	-6.4506333	1.48E-10	9.45E-08
METTL7A	methyltransferase like 7A	-6.6215857	5.40E-08	1.58E-05
LMOD1B	leiomodin 1b (smooth muscle)	-7.062909	2.39E-13	2.48E-10
IMPACT	impact RWD domain protein	-7.5613604	8.73E-22	2.38E-18
PVALB6	parvalbumin 6	-7.930924	2.90E-13	2.87E-10
SHISA4	shisa family member 4	-8.5997904	7.23E-30	3.93E-26
FBXO43	F-box protein 43	8.29402034	1.90E-07	4.76E-05
GGACT.1	gamma-glutamylamine cyclotransferase, tandem duplicate 1	8.06484833	5.19E-11	3.65E-08
GGACT.2	gamma-glutamylamine cyclotransferase, tandem duplicate 2	7.37013805	1.12E-15	1.57E-12
CCL39.3	chemokine (C-C motif) ligand 39, duplicate 3	7.13772243	2.17E-10	1.35E-07
RRM2	ribonucleotide reductase M2 polypeptide	6.00440664	4.09E-13	3.87E-10
CA15B	carbonic anhydrase XVb	5.36968293	7.42E-10	3.94E-07
CXXC1B	CXXC finger protein 1b	5.33419367	1.83E-13	1.99E-10
MEP1A.1	meprin A, alpha (PABA peptide hydrolase), tandem duplicate 1	3.84375541	7.43E-09	3.05E-06
CD28	CD28 molecule	3.22087295	1.89E-08	6.75E-06
IGHV1-4	immunoglobulin heavy variable 1-4	2.62990227	1.73E-07	4.39E-05
IGIC1S1	immunoglobulin light iota constant 1, s1	2.54514903	3.59E-07	8.05E-05
IGL1C3	immunoglobulin light 1 constant 3	2.4449309	1.79E-08	6.60E-06
RLF	rearranged L-myc fusion	2.36516038	9.47E-10	4.81E-07
GTSE1	G-2 and S-phase expressed 1	2.10723957	9.20E-08	2.44E-05
RPL10	ribosomal protein L10	1.96904191	2.10E-12	1.85E-09
ATP2B3B	ATPase plasma membrane Ca2+ transporting 3b	1.86651153	1.54E-13	1.76E-10
CYP2C9	si:zfos-411a11.2	1.63531733	7.08E-09	2.96E-06
OSTF1	osteoclast stimulating factor 1	1.31130793	8.53E-09	3.37E-06
SEPTIN 15	septin 15	1.22153134	5.16E-08	1.55E-05

References

1. Hoy, D., et al., *The global burden of low back pain: estimates from the Global Burden of Disease 2010 study.* Ann Rheum Dis, 2014. **73**(6): p. 968-74.
2. Katz, J.N., *Lumbar disc disorders and low-back pain: socioeconomic factors and consequences.* J Bone Joint Surg Am, 2006. **88 Suppl 2**: p. 21-4.
3. Dowdell, J., et al., *Intervertebral Disk Degeneration and Repair.* Neurosurgery, 2017. **80**(3S): p. S46-S54.
4. Sambrook, P.N., A.J. MacGregor, and T.D. Spector, *Genetic influences on cervical and lumbar disc degeneration: a magnetic resonance imaging study in twins.* Arthritis Rheum, 1999. **42**(2): p. 366-72.
5. Hirose, Y., et al., *A functional polymorphism in THBS2 that affects alternative splicing and MMP binding is associated with lumbar-disc herniation.* Am J Hum Genet, 2008. **82**(5): p. 1122-9.
6. Yuan, B., et al., *Association analysis between thrombospondin-2 gene polymorphisms and intervertebral disc degeneration in a Chinese Han population.* Medicine (Baltimore), 2018. **97**(2): p. e9586.
7. Xue, J., et al., *Vitamin D receptor gene polymorphisms and risk of intervertebral disc degeneration: An updated meta-analysis based on 23 studies.* Medicine (Baltimore), 2021. **100**(20): p. e25922.
8. Pabalan, N., et al., *Association Between the FokI and ApaI Polymorphisms in the Vitamin D Receptor Gene and Intervertebral Disc Degeneration: A Systematic Review and Meta-Analysis.* Genet Test Mol Biomarkers, 2017. **21**(1): p. 24-32.
9. Munir, S., et al., *Intervertebral Disc Biology: Genetic Basis of Disc Degeneration.* Curr Mol Biol Rep, 2018. **4**(4): p. 143-150.
10. Feng, Y., B. Egan, and J. Wang, *Genetic Factors in Intervertebral Disc Degeneration.* Genes Dis, 2016. **3**(3): p. 178-185.
11. Huang, D., et al., *Association of COL9A3 trp3 polymorphism with intervertebral disk degeneration: a meta-analysis.* BMC Musculoskelet Disord, 2018. **19**(1): p. 381.
12. Wu, H., et al., *Collagen IX gene polymorphisms and lumbar disc degeneration: a systematic review and meta-analysis.* J Orthop Surg Res, 2018. **13**(1): p. 47.
13. Rathod, T.N., et al., *Association between single nucleotide polymorphism in collagen IX and intervertebral disc disease in the Indian population.* Indian J Orthop, 2012. **46**(4): p. 420-6.
14. Diab, M., J.J. Wu, and D.R. Eyre, *Collagen type IX from human cartilage: a structural profile of intermolecular cross-linking sites.* Biochem J, 1996. **314 (Pt 1)**: p. 327-32.
15. van der Rest, M. and R. Mayne, *Type IX collagen proteoglycan from cartilage is covalently cross-linked to type II collagen.* J Biol Chem, 1988. **263**(4): p. 1615-8.
16. Jackson, G.C., et al., *Type IX collagen gene mutations can result in multiple epiphyseal dysplasia that is associated with osteochondritis dissecans and a mild myopathy.* Am J Med Genet A, 2010. **152A**(4): p. 863-9.
17. Noponen-Hietala, N., et al., *Sequence variations in the collagen IX and XI genes are associated with degenerative lumbar spinal stenosis.* Ann Rheum Dis, 2003. **62**(12): p. 1208-14.
18. Liang, C., et al., *Whole-genome sequencing reveals novel genes in ossification of the posterior longitudinal ligament of the thoracic spine in the Chinese population.* J Orthop Surg Res, 2018. **13**(1): p. 324.

19. Boyd, L.M., et al., *Early-onset degeneration of the intervertebral disc and vertebral end plate in mice deficient in type IX collagen.* Arthritis Rheum, 2008. **58**(1): p. 164-71.
20. Witten, P.E. and B.K. Hall, *The Notochord: Development, Evolution and contributions to the vertebral column* 2022, Boca Raton: CRC Press.
21. Symmons, S., *Notochordal and elastic components of the axial skeleton of fishes and their functions in locomotion* J. Zool, 1979. **189**: p. 157-206.
22. Witten, P.E., et al., *Bone without minerals and its secondary mineralization in Atlantic salmon (Salmo salar): the recovery from phosphorus deficiency.* J Exp Biol, 2019. **222**(Pt 3).
23. Schmitz, R.J., *Ultrastructure and function of cellular components of the intercentral joint in the percoid vertebral column.* J Morphol, 1995. **226**(1): p. 1-24.
24. Kague, E., et al., *3D assessment of intervertebral disc degeneration in zebrafish identifies changes in bone density that prime disc disease.* Bone Res, 2021. **9**(1): p. 39.
25. Kague, E. and D. Karasik, *Functional Validation of Osteoporosis Genetic Findings Using Small Fish Models.* Genes (Basel), 2022. **13**(2).
26. Rauner, M., et al., *Perspective of the GEMSTONE Consortium on Current and Future Approaches to Functional Validation for Skeletal Genetic Disease Using Cellular, Molecular and Animal-Modeling Techniques.* Front Endocrinol (Lausanne), 2021.
27. Wopat, S., et al., *Spine Patterning Is Guided by Segmentation of the Notochord Sheath.* Cell Rep, 2018. **22**(8): p. 2026-2038.
28. Rose, P.S., et al., *Thoracolumbar spinal abnormalities in Stickler syndrome.* Spine (Phila Pa 1976), 2001. **26**(4): p. 403-9.
29. Dallas, S.L. and L.F. Bonewald, *Dynamics of the transition from osteoblast to osteocyte.* Ann N Y Acad Sci, 2010. **1192**: p. 437-43.
30. Huitema, L.F., et al., *Entpd5 is essential for skeletal mineralization and regulates phosphate homeostasis in zebrafish.* Proc Natl Acad Sci U S A, 2012. **109**(52): p. 21372-7.
31. Pogoda, H.M., et al., *Direct activation of chordoblasts by retinoic acid is required for segmented centra mineralization during zebrafish spine development.* Development, 2018. **145**(9).
32. Thatcher, J.E. and N. Isoherranen, *The role of CYP26 enzymes in retinoic acid clearance.* Expert Opin Drug Metab Toxicol, 2009. **5**(8): p. 875-86.
33. Lopez-Cuevas, P., et al., *Transformed notochordal cells trigger chronic wounds destabilizing the vertebral column and bone homeostasis.* Dis Model Mech, 2021.
34. Fleisch, H., R.G. Russell, and F. Straumann, *Effect of pyrophosphate on hydroxyapatite and its implications in calcium homeostasis.* Nature, 1966. **212**(5065): p. 901-3.
35. Horowitz, E., J.L. Miller, and L.I. Rose, *Etidronate for hypercalcemia of malignancy and osteoporosis.* Am Fam Physician, 1991. **43**(6): p. 2155-9.
36. Le, H.G., J.E. Dowling, and D.J. Cameron, *Early retinoic acid deprivation in developing zebrafish results in microphthalmia.* Vis Neurosci, 2012. **29**(4-5): p. 219-28.
37. Seargent, J.M., E.A. Yates, and J.H. Gill, *GW9662, a potent antagonist of PPARgamma, inhibits growth of breast tumour cells and promotes the anticancer effects of the PPARgamma agonist rosiglitazone, independently of PPARgamma activation.* Br J Pharmacol, 2004. **143**(8): p. 933-7.

38. Panwar, V., et al., *Multifaceted role of mTOR (mammalian target of rapamycin) signaling pathway in human health and disease.* Signal Transduct Target Ther, 2023. **8**(1): p. 375.
39. Olsen, B.R., *Collagen IX.* Int J Biochem Cell Biol, 1997. **29**(4): p. 555-8.
40. Kamper, M., et al., *Early changes in morphology, bone mineral density and matrix composition of vertebrae lead to disc degeneration in aged collagen IX -/- mice.* Matrix Biol, 2016. **49**: p. 132-143.
41. Budde, B., et al., *Altered integration of matrilin-3 into cartilage extracellular matrix in the absence of collagen IX.* Mol Cell Biol, 2005. **25**(23): p. 10465-78.
42. Gray, R.S., et al., *Loss of col8a1a function during zebrafish embryogenesis results in congenital vertebral malformations.* Dev Biol, 2014. **386**(1): p. 72-85.
43. Inohaya, K., Y. Takano, and A. Kudo, *Production of Wnt4b by floor plate cells is essential for the segmental patterning of the vertebral column in medaka.* Development, 2010. **137**(11): p. 1807-13.
44. Lopez-Baez, J.C., et al., *Wilms Tumor 1b defines a wound-specific sheath cell subpopulation associated with notochord repair.* Elife, 2018. **7**.
45. Orriss, I.R., *Extracellular pyrophosphate: The body's "water softener".* Bone, 2020. **134**: p. 115243.
46. Bagwell, J., et al., *Notochord vacuoles absorb compressive bone growth during zebrafish spine formation.* Elife, 2020. **9**.
47. Li, Z., et al., *Tenascin-C-mediated suppression of extracellular matrix adhesion force promotes entheseal new bone formation through activation of Hippo signalling in ankylosing spondylitis.* Ann Rheum Dis, 2021. **80**(7): p. 891-902.
48. Snijders, B.M.G., M.J.L. Peters, and H.L. Koek, *Ectopic Calcification: What Do We Know and What Is the Way Forward?* J Clin Med, 2023. **12**(11).
49. Wentworth, K.L., U. Masharani, and E.C. Hsiao, *Therapeutic advances for blocking heterotopic ossification in fibrodysplasia ossificans progressiva.* Br J Clin Pharmacol, 2019. **85**(6): p. 1180-1187.
50. Fleisch, H., *Bisphosphonates: mechanisms of action.* Endocr Rev, 1998. **19**(1): p. 80-100.
51. Yi, J., et al., *Lipid metabolism disorder promotes the development of intervertebral disc degeneration.* Biomed Pharmacother, 2023. **166**: p. 115401.
52. Chaput, C.D., M. Siddiqui, and M.D. Rahm, *Obesity and calcification of the ligaments of the spine: a comprehensive CT analysis of the entire spine in a random trauma population.* Spine J, 2019. **19**(8): p. 1346-1353.
53. Patel, P., et al., *Novel Differentially Methylated Regions Identified by Genome-Wide DNA Methylation Analyses Contribute to Racial Disparities in Childhood Obesity.* Genes (Basel), 2023. **14**(5).
54. Hsu, Y.J., et al., *Hyperphosphatemia induces protective autophagy in endothelial cells through the inhibition of Akt/mTOR signaling.* J Vasc Surg, 2015. **62**(1): p. 210-221 e2.
55. Proudfoot, D., et al., *Apoptosis regulates human vascular calcification in vitro: evidence for initiation of vascular calcification by apoptotic bodies.* Circ Res, 2000. **87**(11): p. 1055-62.
56. Westerfield, M., *The zebrafish book. A guide for the laboratory use of zebrafish (Danio rerio).* Vol. 4th Ed. 2000: Univ. of Oregon Press, Eugene
57. Spoorendonk, K.M., et al., *Retinoic acid and Cyp26b1 are critical regulators of osteogenesis in the axial skeleton.* Development, 2008. **135**(22): p. 3765-74.

58. Garcia, J., et al., *Sheath Cell Invasion and Trans-differentiation Repair Mechanical Damage Caused by Loss of Caveolae in the Zebrafish Notochord.* Curr Biol, 2017. **27**(13): p. 1982-1989 e3.
59. Ellett, F., et al., *mpeg1 promoter transgenes direct macrophage-lineage expression in zebrafish.* Blood, 2011. **117**(4): p. e49-56.
60. Hammond, C.L. and S. Schulte-Merker, *Two populations of endochondral osteoblasts with differential sensitivity to Hedgehog signalling.* Development, 2009. **136**(23): p. 3991-4000.
61. Bouxsein, M.L., et al., *Guidelines for assessment of bone microstructure in rodents using micro-computed tomography.* J Bone Miner Res, 2010. **25**(7): p. 1468-86.
62. Kague, E., et al., *Scleraxis genes are required for normal musculoskeletal development and for rib growth and mineralization in zebrafish.* FASEB J, 2019. **33**(8): p. 9116-9130.
63. Kague, E., et al., *Zebrafish sp7 mutants show tooth cycling independent of attachment, eruption and poor differentiation of teeth.* Dev Biol, 2018. **435**(2): p. 176-184.
64. Hayes, A.J., et al., *Spinal deformity in aged zebrafish is accompanied by degenerative changes to their vertebrae that resemble osteoarthritis.* PLoS One, 2013. **8**(9): p. e75787.
65. Poss, K.D., L.G. Wilson, and M.T. Keating, *Heart regeneration in zebrafish.* Science, 2002. **298**(5601): p. 2188-90.
66. Schindelin, J., et al., *Fiji: an open-source platform for biological-image analysis.* Nat Methods, 2012. **9**(7): p. 676-82.
67. De Clercq, A., et al., *The external phenotype-skeleton link in post-hatch farmed Chinook salmon (Oncorhynchus tshawytscha).* J Fish Dis, 2018. **41**(3): p. 511-527.
68. Bensimon-Brito, A., et al., *Revisiting in vivo staining with alizarin red S--a valuable approach to analyse zebrafish skeletal mineralization during development and regeneration.* BMC Dev Biol, 2016. **16**: p. 2.
69. Spurr, A.R., *A low-viscosity epoxy resin embedding medium for electron microscopy.* J Ultrastruct Res, 1969. **26**(1): p. 31-43.
70. Witten, P.E., *Enzyme histochemical characteristics of osteoblasts and mononucleated osteoclasts in a teleost fish with acellular bone (Oreochromis niloticus, Cichlidae).* Cell Tissue Res, 1997. **287**(3): p. 591-9.
71. Apschner, A., et al., *Zebrafish enpp1 mutants exhibit pathological mineralization, mimicking features of generalized arterial calcification of infancy (GACI) and pseudoxanthoma elasticum (PXE).* Dis Model Mech, 2014. **7**(7): p. 811-22.
72. Jin, M., et al., *Involvement of peroxisome proliferator-activated receptor gamma in anticonvulsant activity of alpha-asaronol against pentylenetetrazole-induced seizures in zebrafish.* Neuropharmacology, 2020. **162**: p. 107760.

1. Hoy, D., et al., *The global burden of low back pain: estimates from the Global Burden of Disease 2010 study.* Ann Rheum Dis, 2014. **73**(6): p. 968-74.
2. Katz, J.N., *Lumbar disc disorders and low-back pain: socioeconomic factors and consequences.* J Bone Joint Surg Am, 2006. **88 Suppl 2**: p. 21-4.
3. Dowdell, J., et al., *Intervertebral Disk Degeneration and Repair.* Neurosurgery, 2017. **80**(3S): p. S46-S54.

4. Sambrook, P.N., A.J. MacGregor, and T.D. Spector, *Genetic influences on cervical and lumbar disc degeneration: a magnetic resonance imaging study in twins.* Arthritis Rheum, 1999. **42**(2): p. 366-72.
5. Hirose, Y., et al., *A functional polymorphism in THBS2 that affects alternative splicing and MMP binding is associated with lumbar-disc herniation.* Am J Hum Genet, 2008. **82**(5): p. 1122-9.
6. Yuan, B., et al., *Association analysis between thrombospondin-2 gene polymorphisms and intervertebral disc degeneration in a Chinese Han population.* Medicine (Baltimore), 2018. **97**(2): p. e9586.
7. Pabalan, N., et al., *Association Between the FokI and ApaI Polymorphisms in the Vitamin D Receptor Gene and Intervertebral Disc Degeneration: A Systematic Review and Meta-Analysis.* Genet Test Mol Biomarkers, 2017. **21**(1): p. 24-32.
8. Xue, J., et al., *Vitamin D receptor gene polymorphisms and risk of intervertebral disc degeneration: An updated meta-analysis based on 23 studies.* Medicine (Baltimore), 2021. **100**(20): p. e25922.
9. Munir, S., et al., *Intervertebral Disc Biology: Genetic Basis of Disc Degeneration.* Curr Mol Biol Rep, 2018. **4**(4): p. 143-150.
10. Feng, Y., B. Egan, and J. Wang, *Genetic Factors in Intervertebral Disc Degeneration.* Genes Dis, 2016. **3**(3): p. 178-185.
11. Huang, D., et al., *Association of COL9A3 trp3 polymorphism with intervertebral disk degeneration: a meta-analysis.* BMC Musculoskelet Disord, 2018. **19**(1): p. 381.
12. Wu, H., et al., *Collagen IX gene polymorphisms and lumbar disc degeneration: a systematic review and meta-analysis.* J Orthop Surg Res, 2018. **13**(1): p. 47.
13. Rathod, T.N., et al., *Association between single nucleotide polymorphism in collagen IX and intervertebral disc disease in the Indian population.* Indian J Orthop, 2012. **46**(4): p. 420-6.
14. Diab, M., J.J. Wu, and D.R. Eyre, *Collagen type IX from human cartilage: a structural profile of intermolecular cross-linking sites.* Biochem J, 1996. **314 (Pt 1)**: p. 327-32.
15. van der Rest, M. and R. Mayne, *Type IX collagen proteoglycan from cartilage is covalently cross-linked to type II collagen.* J Biol Chem, 1988. **263**(4): p. 1615-8.
16. Jackson, G.C., et al., *Type IX collagen gene mutations can result in multiple epiphyseal dysplasia that is associated with osteochondritis dissecans and a mild myopathy.* Am J Med Genet A, 2010. **152A**(4): p. 863-9.
17. Noponen-Hietala, N., et al., *Sequence variations in the collagen IX and XI genes are associated with degenerative lumbar spinal stenosis.* Ann Rheum Dis, 2003. **62**(12): p. 1208-14.
18. Liang, C., et al., *Whole-genome sequencing reveals novel genes in ossification of the posterior longitudinal ligament of the thoracic spine in the Chinese population.* J Orthop Surg Res, 2018. **13**(1): p. 324.
19. Boyd, L.M., et al., *Early-onset degeneration of the intervertebral disc and vertebral end plate in mice deficient in type IX collagen.* Arthritis Rheum, 2008. **58**(1): p. 164-71.
20. Witten, P.E. and B.K. Hall, *The Notochord: Development, Evolution and contributions to the vertebral column* 2022, Boca Raton: CRC Press.
21. Symmons, S., *Notochordal and elastic components of the axial skeleton of fishes and their functions in locomotion.* Journal of Zoology, 1979. **189**(2): p. 157-206.
22. Witten, P.E., et al., *Bone without minerals and its secondary mineralization in Atlantic salmon (Salmo salar): the recovery from phosphorus deficiency.* J Exp Biol, 2019. **222**(Pt 3).

23. Schmitz, R.J., *Ultrastructure and function of cellular components of the intercentral joint in the percoid vertebral column.* J Morphol, 1995. **226**(1): p. 1-24.
24. Kague, E., et al., *3D assessment of intervertebral disc degeneration in zebrafish identifies changes in bone density that prime disc disease.* Bone Res, 2021. **9**(1): p. 39.
25. Kague, E. and D. Karasik, *Functional Validation of Osteoporosis Genetic Findings Using Small Fish Models.* Genes (Basel), 2022. **13**(2).
26. Rauner, M., et al., *Perspective of the GEMSTONE Consortium on Current and Future Approaches to Functional Validation for Skeletal Genetic Disease Using Cellular, Molecular and Animal-Modeling Techniques.* Front Endocrinol (Lausanne), 2021. **12**: p. 731217.
27. Wopat, S., et al., *Spine Patterning Is Guided by Segmentation of the Notochord Sheath.* Cell Rep, 2018. **22**(8): p. 2026-2038.
28. Rose, P.S., et al., *Thoracolumbar spinal abnormalities in Stickler syndrome.* Spine (Phila Pa 1976), 2001. **26**(4): p. 403-9.
29. Huitema, L.F., et al., *Entpd5 is essential for skeletal mineralization and regulates phosphate homeostasis in zebrafish.* Proc Natl Acad Sci U S A, 2012. **109**(52): p. 21372-7.
30. Pogoda, H.M., et al., *Direct activation of chordoblasts by retinoic acid is required for segmented centra mineralization during zebrafish spine development.* Development, 2018. **145**(9).
31. Thatcher, J.E. and N. Isoherranen, *The role of CYP26 enzymes in retinoic acid clearance.* Expert Opin Drug Metab Toxicol, 2009. **5**(8): p. 875-86.
32. Lopez-Cuevas, P., et al., *Transformed notochordal cells trigger chronic wounds in zebrafish, destabilizing the vertebral column and bone homeostasis.* Dis Model Mech, 2021. **14**(3).
33. Fleisch, H., R.G. Russell, and F. Straumann, *Effect of pyrophosphate on hydroxyapatite and its implications in calcium homeostasis.* Nature, 1966. **212**(5065): p. 901-3.
34. Horowitz, E., J.L. Miller, and L.I. Rose, *Etidronate for hypercalcemia of malignancy and osteoporosis.* Am Fam Physician, 1991. **43**(6): p. 2155-9.
35. Le, H.G., J.E. Dowling, and D.J. Cameron, *Early retinoic acid deprivation in developing zebrafish results in microphthalmia.* Vis Neurosci, 2012. **29**(4-5): p. 219-28.
36. Seargent, J.M., E.A. Yates, and J.H. Gill, *GW9662, a potent antagonist of PPARgamma, inhibits growth of breast tumour cells and promotes the anticancer effects of the PPARgamma agonist rosiglitazone, independently of PPARgamma activation.* Br J Pharmacol, 2004. **143**(8): p. 933-7.
37. Panwar, V., et al., *Multifaceted role of mTOR (mammalian target of rapamycin) signaling pathway in human health and disease.* Signal Transduct Target Ther, 2023. **8**(1): p. 375.
38. Olsen, B.R., *Collagen IX.* Int J Biochem Cell Biol, 1997. **29**(4): p. 555-8.
39. Kamper, M., et al., *Early changes in morphology, bone mineral density and matrix composition of vertebrae lead to disc degeneration in aged collagen IX -/- mice.* Matrix Biol, 2016. **49**: p. 132-143.
40. Budde, B., et al., *Altered integration of matrilin-3 into cartilage extracellular matrix in the absence of collagen IX.* Mol Cell Biol, 2005. **25**(23): p. 10465-78.
41. Gray, R.S., et al., *Loss of col8a1a function during zebrafish embryogenesis results in congenital vertebral malformations.* Dev Biol, 2014. **386**(1): p. 72-85.

42. Inohaya, K., Y. Takano, and A. Kudo, *Production of Wnt4b by floor plate cells is essential for the segmental patterning of the vertebral column in medaka.* Development, 2010. **137**(11): p. 1807-13.
43. Lopez-Baez, J.C., et al., *Wilms Tumor 1b defines a wound-specific sheath cell subpopulation associated with notochord repair.* Elife, 2018. **7**.
44. Orriss, I.R., *Extracellular pyrophosphate: The body's "water softener".* Bone, 2020. **134**: p. 115243.
45. Bagwell, J., et al., *Notochord vacuoles absorb compressive bone growth during zebrafish spine formation.* Elife, 2020. **9**.
46. Snijders, B.M.G., M.J.L. Peters, and H.L. Koek, *Ectopic Calcification: What Do We Know and What Is the Way Forward?* J Clin Med, 2023. **12**(11).
47. Wentworth, K.L., U. Masharani, and E.C. Hsiao, *Therapeutic advances for blocking heterotopic ossification in fibrodysplasia ossificans progressiva.* Br J Clin Pharmacol, 2019. **85**(6): p. 1180-1187.
48. Fleisch, H., *Bisphosphonates: mechanisms of action.* Endocr Rev, 1998. **19**(1): p. 80-100.
49. Yi, J., et al., *Lipid metabolism disorder promotes the development of intervertebral disc degeneration.* Biomed Pharmacother, 2023. **166**: p. 115401.
50. Chaput, C.D., M. Siddiqui, and M.D. Rahm, *Obesity and calcification of the ligaments of the spine: a comprehensive CT analysis of the entire spine in a random trauma population.* Spine J, 2019. **19**(8): p. 1346-1353.
51. Patel, P., et al., *Novel Differentially Methylated Regions Identified by Genome-Wide DNA Methylation Analyses Contribute to Racial Disparities in Childhood Obesity.* Genes (Basel), 2023. **14**(5).
52. Kague, E., et al., *Standardization of bone morphometry and mineral density assessments in zebrafish and other small laboratory fishes using X-ray radiography and micro-computed tomography.* J Bone Miner Res, 2024. **39**(12): p. 1695-1710.
53. Kague, E., et al., *Zebrafish sp7 mutants show tooth cycling independent of attachment, eruption and poor differentiation of teeth.* Dev Biol, 2018. **435**(2): p. 176-184.
54. Hayes, A.J., et al., *Spinal deformity in aged zebrafish is accompanied by degenerative changes to their vertebrae that resemble osteoarthritis.* PLoS One, 2013. **8**(9): p. e75787.
55. Poss, K.D., L.G. Wilson, and M.T. Keating, *Heart regeneration in zebrafish.* Science, 2002. **298**(5601): p. 2188-90.
56. De Clercq, A., et al., *The external phenotype-skeleton link in post-hatch farmed Chinook salmon (Oncorhynchus tshawytscha).* J Fish Dis, 2018. **41**(3): p. 511-527.
57. Bensimon-Brito, A., et al., *Revisiting in vivo staining with alizarin red S--a valuable approach to analyse zebrafish skeletal mineralization during development and regeneration.* BMC Dev Biol, 2016. **16**: p. 2.
58. Schindelin, J., et al., *Fiji: an open-source platform for biological-image analysis.* Nat Methods, 2012. **9**(7): p. 676-82.
59. Spurr, A.R., *A low-viscosity epoxy resin embedding medium for electron microscopy.* J Ultrastruct Res, 1969. **26**(1): p. 31-43.
60. Witten, P.E., *Enzyme histochemical characteristics of osteoblasts and mononucleated osteoclasts in a teleost fish with acellular bone (Oreochromis niloticus, Cichlidae).* Cell Tissue Res, 1997. **287**(3): p. 591-9.
61. Apschner, A., et al., *Zebrafish enpp1 mutants exhibit pathological mineralization, mimicking features of generalized arterial calcification of infancy (GACI) and pseudoxanthoma elasticum (PXE).* Dis Model Mech, 2014. **7**(7): p. 811-22.

62. Jin, M., et al., *Involvement of peroxisome proliferator-activated receptor gamma in anticonvulsant activity of alpha-asaronol against pentylenetetrazole-induced seizures in zebrafish.* Neuropharmacology, 2020. **162**: p. 107760.

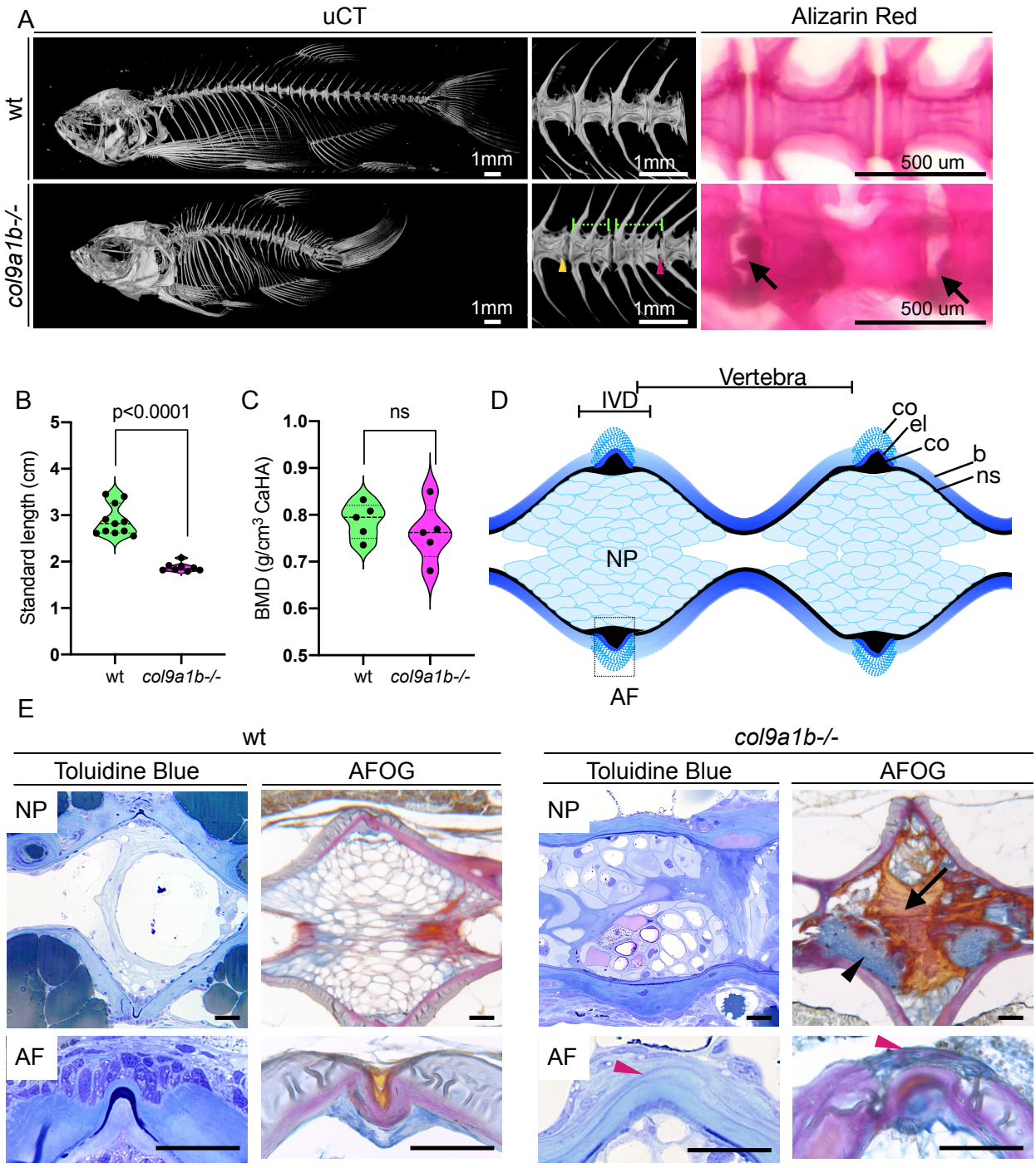


Figure 1. Vertebral fusions in zebrafish *col9a1b* mutants. A) µCT of adult zebrafish. Higher resolution images are presented on the right panel to show vertebral fusions (dashed green lines). Endplate sclerosis (yellow arrowhead); IVD mineralization (magenta arrowhead). Scale bars= 1mm. B) Standard fish length (wt n=11; *col9a1b-/-* n=8). C) Cortical bone mineral density (BMD) (wt n=5; *col9a1b-/-* n=5). Nonparametric T-tests and Mann-Whitney test (B and C). All significant p values are as indicated. D) Schematic of a histological section of the vertebral column of zebrafish not at the middle plane showing two consecutive IVDs. IVD = intervertebral disc; NP = nucleus pulposus; AF = annulus fibrosus; co = collagen layers; el = elastin layer; b = bone; ns = notochord sheath. E) Histological sections of zebrafish IVDs stained with Toluidine blue or AFOG. Black arrow (fibrosis), magenta arrowheads (abnormal collagen layer), black arrowhead (abnormal cartilage trapped in the NP). Scale Bars= 50um.

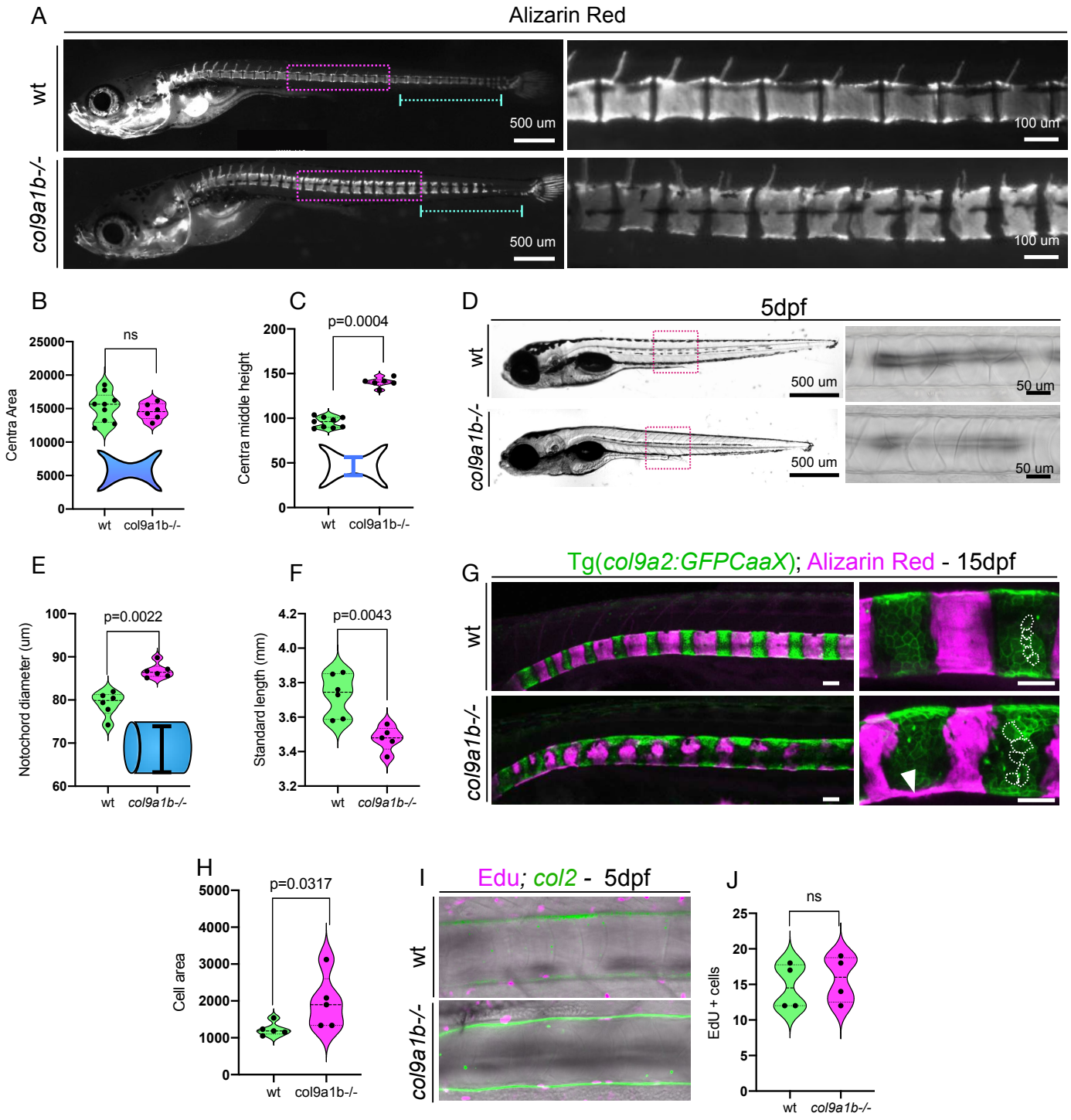


Figure 2. Vertebral fusions are preceded by ectopic expression of mineralization markers during vertebral segmentation. A) Live alizarin red of same SL wt and *col9a1-/-*. Higher magnification of same vertebral regions (magenta dashed box) is shown. Note all vertebral segments formed in the wt and delayed formation in *col9a1b-/-* (cyan dashed lines). Scale bars are indicated. B) Centrae areas (wt n= 9; *col9a1b-/-* n= 6). C) Middle height of centrae (wt n= 9; *col9a1b-/-* n= 6). D) Transmitted light image of 5dpf larvae. higher. Magnification of the notochord region is hown on the right panel. E) Notochord diameter. F) Larvae SL (standard length). G) 15dpf wt and *col9a1b-/-* with notochord sheath epithelium labelled with Tg(*col9a2:GFPcaaX*) and live stained with Alizarin Red. Higher magnification shown in the right panel. White arrowhead (ectopic mineralization), blue arrowhead (higher shape distortion in the middle of chordacentrae), white dashed lines (notochord sheath cell perimeters). H) Cell areas of the notochord epithelium of wt (n=5) and *col9a1b-/-* (n=5). I) Cell proliferation assessed through EdU labelling. J) Quantification of EdU+ cells in the notochord region. Nonparametric T-tests and Mann-Whitney test, p value is annotated.

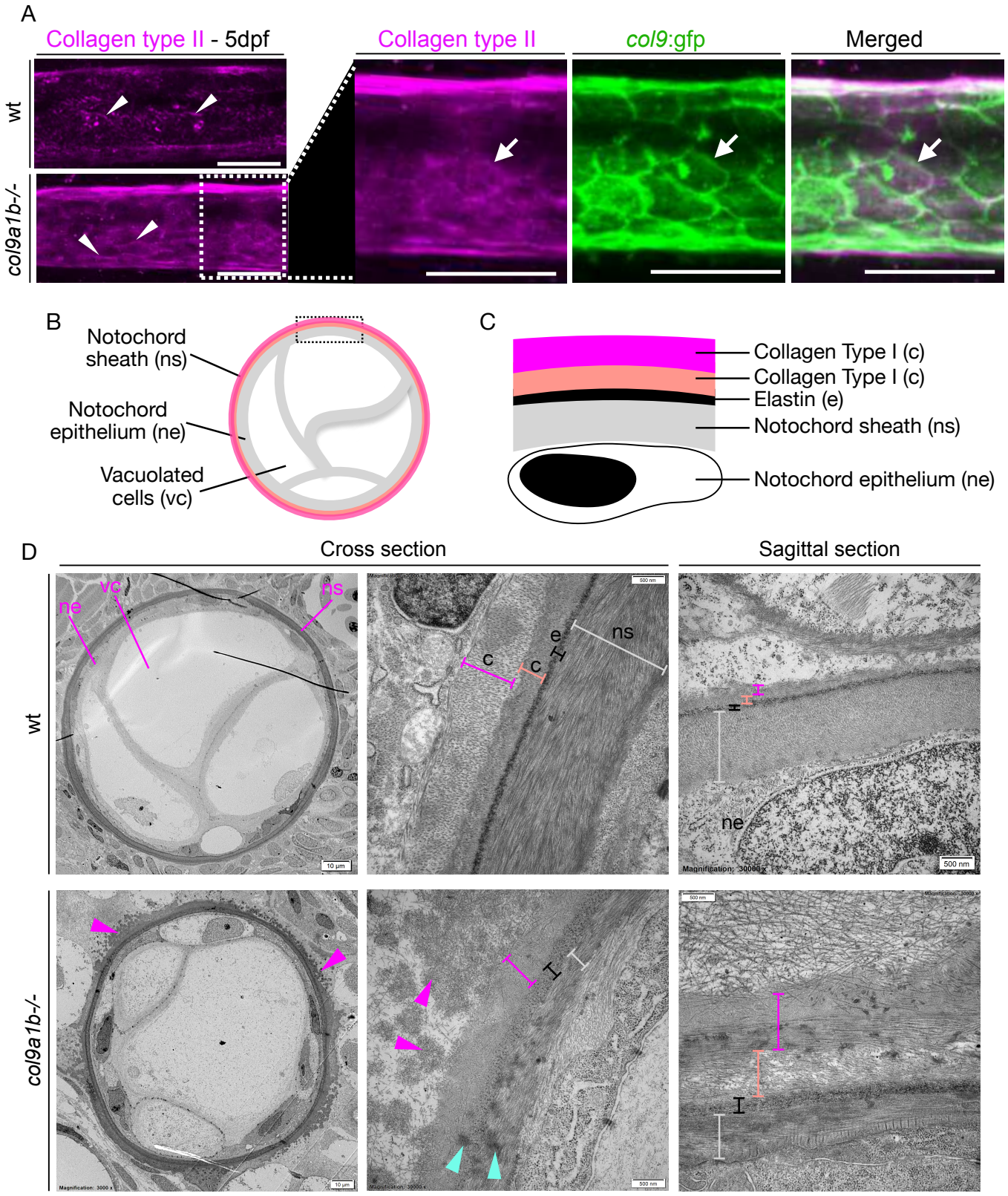


Figure 3. Lack of *col9a1b* causes structural impairment of the notochord sheath. A) Immunofluorescence for collagen type II in 5dpf larvae. Note higher signal adjacent to notochord epithelium cells (arrowheads). Higher magnification of mutant notochord is shown on the right panel, to highlight positioning of each notochord epithelium cell through Tg(*col9a1:gfp)* overlapped with immunostaining for collagen type II. Arrows point to the edge of notochord epithelium cell, showing increased deposition of collagen type II. Scale bars = 50µm. B) Diagram of a cross section through the notochord. The notochord is formed by the notochord sheath (ns), notochord epithelium (ne) and vacuolated cells. C) Diagram of a region of the notochord (dashed square in B) in higher magnification. From the outside to the inside of the notochord, we detect the collagen type I layer (c), the elastin layer (e), the notochord sheath (ns) and the epithelium layer (e). D) TEM of cross sections and sagittal sections of the wt and *col9a1b-/-* notochords. Scale bars are indicated in each picture.

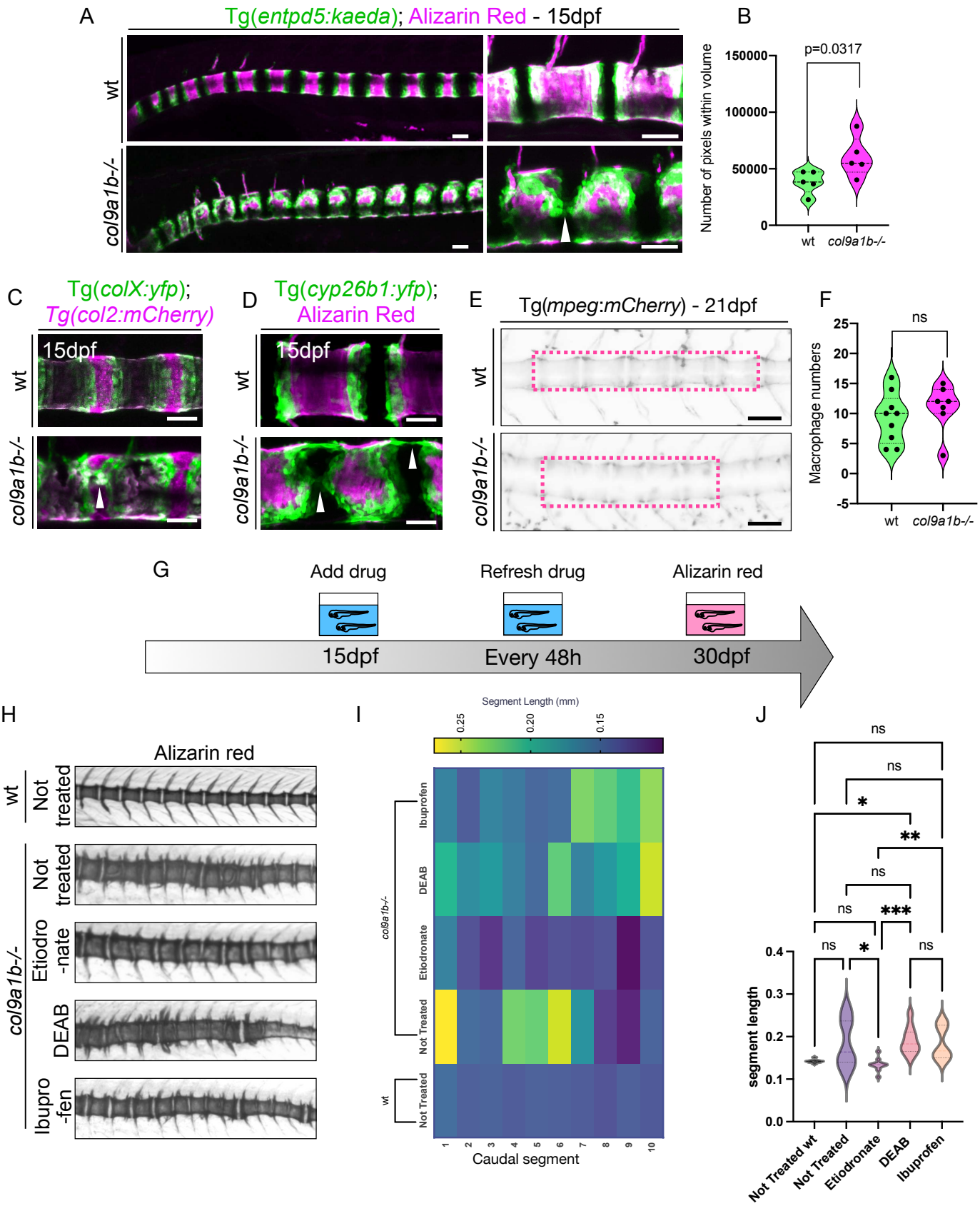

A
Tg(entpd5:kaeda); Alizarin Red - 15dpf
wt
col9a1b-/-
B
p=0.0317
Number of pixels within volume
150000
100000
50000
0
wt
col9a1b-/-
C
Tg(colX:yfp);
Tg(col2:mCherry)
15dpf
wt
col9a1b-/-
D
Tg(cyp26b1:yfp);
Alizarin Red
15dpf
wt
col9a1b-/-
E
Tg(mpeg:mCherry) - 21dpf
wt
col9a1b-/-
F
ns
Macrophage numbers
25
20
15
10
5
0
-5
wt
col9a1b-/-
G
Add drug
Refresh drug
Alizarin red
15dpf
Every 48h
30dpf
H
Alizarin red
wt
Not treated
col9a1b-/-
Not treated
Etiodro -nate
DEAB
Ibupro -fen
I
Segment Length (mm)
0.25
0.20
0.15
col9a1b-/-
Ibuprofen
DEAB
Etiodronate
Not Treated
wt
Not Treated
1
2
3
4
5
6
7
8
9
10
Caudal segment
J
ns
ns
*
**
ns
ns
***
ns
*
ns
segment length
0.4
0.3
0.2
0.1
0.0
Not Treated wt
Not Treated
Etiodronate
DEAB
Ibuprofen

Figure 4. *col9a1b* is important to maintain cellular integrity within the notochord sheath epithelium. A) 15dpf wt and *col9a1b-/-* carrying Tg(*entpd5:kaeda*) and live stained with Alizarin Red (mineralised bones). Note ectopic expression of *entpd5* in chordoblasts (arrowhead) within the IVD region. B) Quantification of volume occupied by *entpd5* positive cells of the notochord epithelium of wt (n=5) and *col9a1b-/-* (n=5). Nonparametric T-tests and Mann-Whitney test, p value is annotated. C) 15dpf wt and col9a1b-/- carrying Tg*(colX:yfp*) (mineralization marker) and Tg(*col2:mCerry*) Noce ectopic expression of colX in chordoblasts within the IVD (arrowhead). D) 15dpf wt and col9a1b-/- carrying Tg(*cyp26b1:yfp*) (retinoic signalling pathway,) and live stained with Alizarin Red (mineralised bones). Note ectopic expression of *cyp26 (*arrowheads*)*. E) 21 dpf wt and *col9a1b-/-* with macrophages labelled through Tg(*mpeg:mCherry*). Macrophages were counted within ten centrae (five centrae indication with magenta dashed box). F) Macrophage numbers in centrae of wt (n=9) and *col9a1b-/-* (n=7). G) Representative schematics of drug treatment (Etiodronate (100µm), Diethylaminobenzaldehyde (DEAB)(10µM) and ibuprofen (10µM). Drug treatment started at 15dpf and finished at 30dpf. Drug solution was refreshed every 48h. Fish were culled and fixed at 3dpf followed by Alizarin Red Staining and imaging. H) Images of wt and drug treated fish at 30dpf stained with Alizarin Red S. I) Fusions of the caudal vertebral segments were detected through measurement of length of the segments. J) Graph showing segment lengths and respective drug treatments. (B, F) Nonparametric T-tests and Mann-Whitney test, all significant p values are as indicated. (J) Non-parametric ANOVA, Kruskal-Wallis, Dunn's multiple comparisons test (*$p<0.5$; **$p<0.05$; ***$p<0.005$). Scale bars = 50µm.

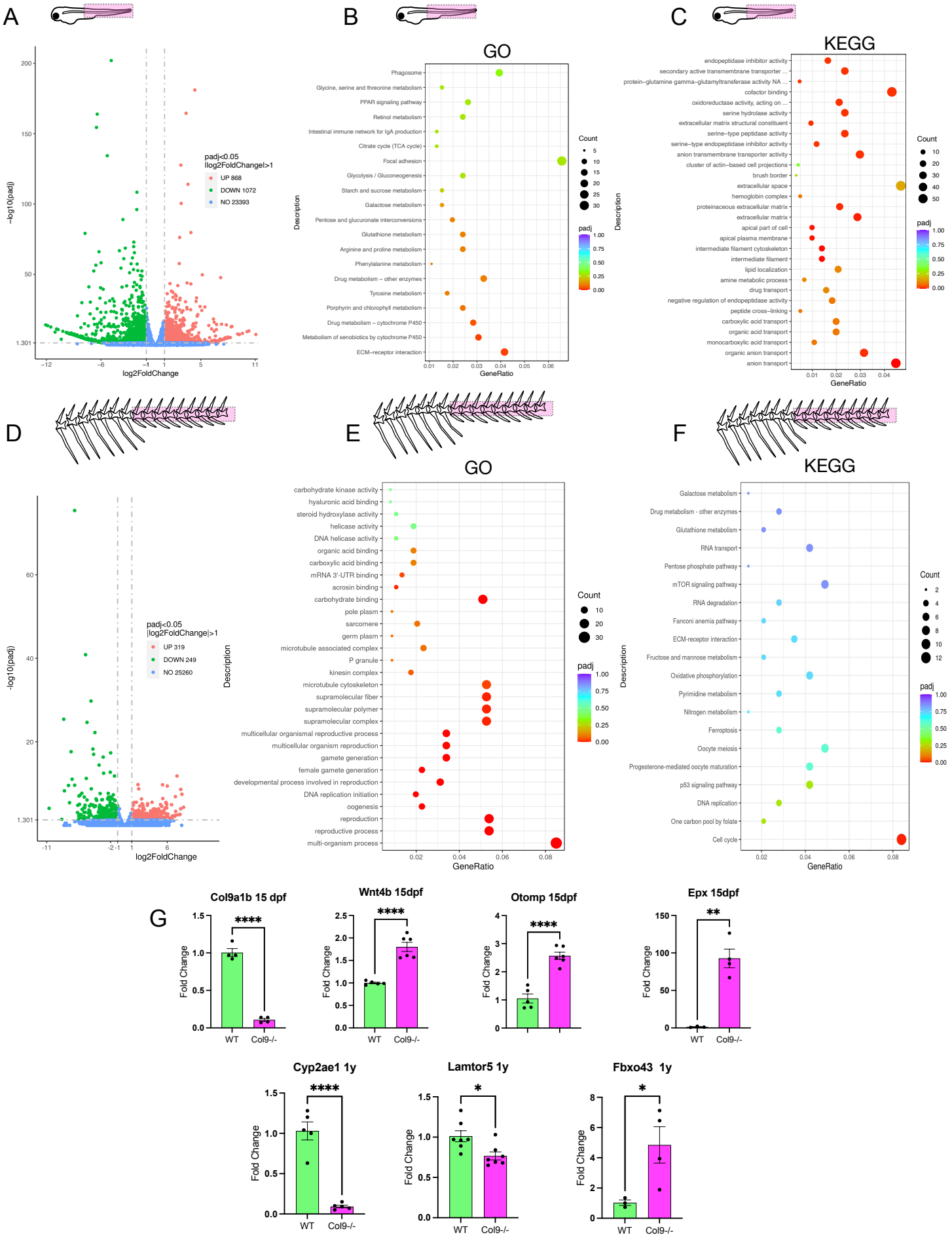

A
B
C
GO
KEGG
padj<0.05
|log2FoldChange|>1
UP 868
DOWN 1072
NO 23393
−log10(padj)
log2FoldChange
Description
GeneRatio
Count
padj
Phagosome
Glycine, serine and threonine metabolism
PPAR signaling pathway
Retinol metabolism
Intestinal immune network for IgA production
Citrate cycle (TCA cycle)
Focal adhesion
Glycolysis / Gluconeogenesis
Starch and sucrose metabolism
Galactose metabolism
Pentose and glucuronate interconversions
Glutathione metabolism
Arginine and proline metabolism
Phenylalanine metabolism
Drug metabolism – other enzymes
Tyrosine metabolism
Porphyrin and chlorophyll metabolism
Drug metabolism – cytochrome P450
Metabolism of xenobiotics by cytochrome P450
ECM–receptor interaction
endopeptidase inhibitor activity
secondary active transmembrane transporter ...
protein–glutamine gamma–glutamyltransferase activity NA ...
cofactor binding
oxidoreductase activity, acting on ...
serine hydrolase activity
extracellular matrix structural constituent
serine–type peptidase activity
serine–type endopeptidase inhibitor activity
anion transmembrane transporter activity
cluster of actin–based cell projections
brush border
extracellular space
hemoglobin complex
proteinaceous extracellular matrix
extracellular matrix
apical part of cell
apical plasma membrane
intermediate filament cytoskeleton
intermediate filament
lipid localization
amine metabolic process
drug transport
negative regulation of endopeptidase activity
peptide cross–linking
carboxylic acid transport
organic acid transport
monocarboxylic acid transport
organic anion transport
anion transport
D
E
F
GO
KEGG
padj<0.05
|log2FoldChange|>1
UP 319
DOWN 249
NO 25260
carbohydrate kinase activity
hyaluronic acid binding
steroid hydroxylase activity
helicase activity
DNA helicase activity
organic acid binding
carboxylic acid binding
mRNA 3'-UTR binding
acrosin binding
carbohydrate binding
pole plasm
sarcomere
germ plasm
microtubule associated complex
P granule
kinesin complex
microtubule cytoskeleton
supramolecular fiber
supramolecular polymer
supramolecular complex
multicellular organismal reproductive process
multicellular organism reproduction
gamete generation
female gamete generation
developmental process involved in reproduction
DNA replication initiation
oogenesis
reproduction
reproductive process
multi-organism process
Galactose metabolism
Drug metabolism - other enzymes
Glutathione metabolism
RNA transport
Pentose phosphate pathway
mTOR signaling pathway
RNA degradation
Fanconi anemia pathway
ECM-receptor interaction
Fructose and mannose metabolism
Oxidative phosphorylation
Pyrimidine metabolism
Nitrogen metabolism
Ferroptosis
Oocyte meiosis
Progesterone-mediated oocyte maturation
p53 signaling pathway
DNA replication
One carbon pool by folate
Cell cycle
G
Col9a1b 15 dpf
Wnt4b 15dpf
Otomp 15dpf
Epx 15dpf
Cyp2ae1 1y
Lamtor5 1y
Fbxo43 1y
Fold Change
WT
Col9-/-

Figure 5. Transcriptomic analysis suggests lipid metabolism and mTOR pathways in ectopic mineralization of *col9a1b-/-*. A) Volcano plot showing differentially up (green dots) and down (red dots) regulated genes between wt and *col9a1b*-/- at 15 dpf. B) Gene ontology (GO) enrichment analysis of biological processes differentially expressed genes (DEGs) between wt and *col9a1b*-/- at 15 dpf. C) Kyoto Encyclopedia of Genes and Genomes (KEGG) pathway enrichment analysis of differentially expressed genes (DEGs) between wt and *col9a1b*-/- at 15 dpf. D) Volcano plot showing differentially up (green dots) and down (red dots) regulated genes between wt and *col9a1b*-/- at 1 year-old. E) Gene ontology (GO) enrichment analysis of biological processes differentially expressed genes (DEGs) between wt and *col9a1b*-/- at 1 year-old. F) Kyoto Encyclopaedia of Genes and Genomes (KEGG) pathway enrichment analysis of differentially expressed genes (DEGs) between wt and *col9a1b*-/- at 1 year-old. G) qPCR for some of the up-down regulated genes at 15dpf and 1 year-old. Unpaired t-test was used. Numbers of samples are as displayed in the graphs.

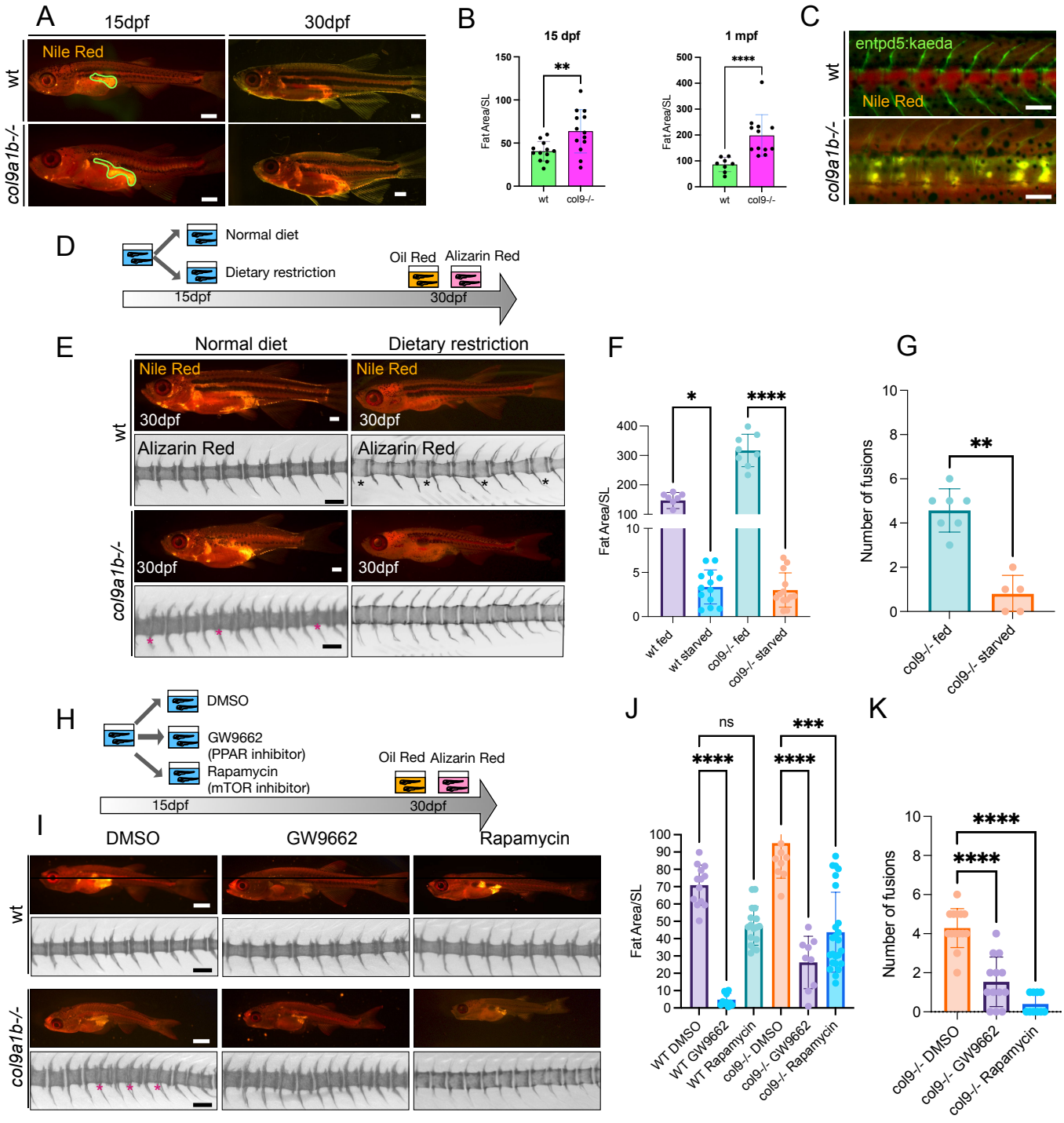

A
15dpf
30dpf
Nile Red
wt
col9a1b-/-
B
15 dpf
1 mpf
Fat Area/SL
**
****
wt
col9-/-
C
entpd5:kaeda
Nile Red
wt
col9a1b-/-
D
Normal diet
Dietary restriction
Oil Red
Alizarin Red
15dpf
30dpf
E
Normal diet
Dietary restriction
Nile Red
Alizarin Red
30dpf
wt
col9a1b-/-
F
Fat Area/SL
*
****
wt fed
wt starved
col9-/- fed
col9-/- starved
G
Number of fusions
**
col9-/- fed
col9-/- starved
H
DMSO
GW9662
(PPAR inhibitor)
Rapamycin
(mTOR inhibitor)
Oil Red
Alizarin Red
15dpf
30dpf
I
DMSO
GW9662
Rapamycin
wt
col9a1b-/-
J
ns
***
****
Fat Area/SL
WT DMSO
WT GW9662
WT Rapamycin
col9-/- DMSO
col9-/- GW9662
col9-/- Rapamycin
K
Number of fusions
****
col9-/- DMSO
col9-/- GW9662
col9-/- Rapamycin

Figure 6. Modulating fat in *col9a1b-/-* partially ameliorates ligament ectopic mineralization. A) Nile Red staining lipids in wt and *col9a1b-/-* at 15dpf and 30dpf. Visceral fat was quantified by drawing around the fat area and quantifying pixel numbers. B) Graph of quantification of visceral fat at 15dpf and 30 dpf (1mpf). C) wt and col9a1b carrying Tg(entpd5:kaeda) and live stained with Nile Red. Note fat droplets around the vertebral column in mutants. D) Schematics illustrating dietary regimen starting at 15dpf and ending at 30dpf, followed by live Nile Red Red Staining and ex-vivo Alizarin Red staining. E) wt and *col9a1b-/-* stained with Nile Red and Alizarin Red Staining at 30dpf. Asterisks in wt undergone dietary restriction, and Alizarin Red, show less mineralised centrae. Magenta asterisks in col9a1b normal diet, alizarin red, point to fused vertebral centrae. F) Graph of quantification of visceral fat area in wt and col9a1b-/- under normal and dietary restriction regimen. G) Quantification of vertebral centrae fusions in the caudal region at 30dpf, after dietary regimen. H) Schematics illustrating drug treatment (GW9662) and Rapamycin starting at 15dpf and ending at 30dpf, followed by live Nile Red Red Staining and ex-vivo Alizarin Red staining. I) wt and *col9a1b-/-* stained with Nile Red and Alizarin Red Staining at 30dpf. Magenta asterisks in *col9a1b* DMSO, alizarin red, point to fused vertebral centrae. J) Graph of quantification of visceral fat area in wt and *col9a1b-/-* subjected to respective drug treatment. K) Quantification of vertebral centrae fusions in the caudal region at 30dpf, after drug treatment. Scale bars = 100µm. (B, G) Mann-Whitney test. (F,J) Non-parametric ANOVA with Kruskal-Wallis test. (K) Ordinary one-way ANOVA. (*$p<0.5$; **$p<0.05$; ***$p<0.005$; **** $p<0.0005$)

Supplementary Files

This is a list of supplementary files associated with this preprint. Click to download.

- SupTable1.xlsx
- Supplementaryinfocombined.pdf